https://doi.org/10.7494/geom.2023.17.5.107

Noura Zoraa[1], Mohammed Raji[2], Hassan El Hadi[3], Soufiane Maimouni[4], Hicham Si Mhamdi[5], Aicha Reddad[6], Ghalem Zahour[7], Achraf Ait-Yazza[8]

Mapping and Assessment of Geological Lineaments with the Contribution of Earth Observation Data: A Case Study of the Zaer Granite Massif, Western Moroccan Meseta

Abstract: The Zaer granitic massif is one of the most important Variscan granitoids in the Central Zone of the Western Moroccan Meseta. It is characterized by a deformation which is manifested by a network of fractures of different scales. Thanks to the technology currently available, many geological studies rely heavily on the mapping of geological lineaments, especially in structural geology. This has become more reliable with access to earth observation data using optical and radar sensors as well as the various remote sensing techniques. Therefore, the objective of this work is to determine the potential of Landsat 8, ASTER, Sentinel 2 and radar Sentinel 1 datasets using the automatic method to extract lineaments. Furthermore, this work focuses on quantitative lineament analysis to determine lineament trends and subsequently compare them with global and regional tectonic movement trends. The lineaments obtained through different satellite images were validated by including the shaded relief maps, the slope map, the correlation with the pre-existing faults in the geological maps as well as the field investigation. Comparison of these results indicates that Sentinel 1 imagery provides a better correlation between automated extraction lineaments and major fault zones. Thus, Sentinel 1 data is more effective in mapping geological lineaments. The final lineament map obtained from the VH and VV polarizations shows two major fault systems, mainly oriented NE-SW and NW-SE to NNW-SSE.

Keywords: lineament extraction, Landsat 8, ASTER, Sentinel, Zaer

Received: 24 November 2022; accepted: 12 July 2023

[1] Hassan II University of Casablanca, Faculty of Sciences Ben M'sick, Laboratory of Applied Geology, Geoinformatics and Environment, Casablanca, Morocco,
email: zonoura@gmail.com (corresponding author), https://orcid.org/0000-0002-7527-9443
[2] Hassan II University of Casablanca, Casablanca, Morocco, email: mhedraji@gmail.com
[3] Hassan II University of Casablanca, Casablanca, Morocco, email: elhadihas@gmail.com
[4] Hassan II University of Casablanca, Casablanca, Morocco, email: soufiane.maimouni@gmail.com
[5] Moulay Ismail University, Errachidia, Morocco, email: hicham.simhamdi@gmail.com
[6] Cadi Ayyad University, Marrakesh, Morocco, email: aicharedd@gmail.com
[7] Hassan II University of Casablanca, Casablanca, Morocco, email: gh_zahour@yahoo.fr
[8] Hassan II University of Casablanca, Casablanca, Morocco, email: achraf.aityazza@gmail.com

1. Introduction

In recent decades, lineament extraction and analysis have been widely used by geologists [1–4]. It is an important indicator for describing tectonic events and their resulting fractures throughout geological history at different scales [5]. The lineament corresponds to the linear features that can be picked in satellite images [6], and can be a representation of a subsurface phenomenon [7–9]. In geological studies, lineaments are generally described as fractures, faults, joints, or boundaries between geological formations [10, 11]. Other types of lineaments can be geomorphological implications [12, 13] or artificial objects (road, bridge, etc.) [14, 15]. There are three essential approaches to extracting geological lineaments using remote sensing data: (i) manual method [13, 16]; (ii) semi-automatic method [17, 18], and (iii) automatic method [19–24]. Therefore, the manual and semi-automatic methods were influenced by the expertise of the interpreter, but the automatic approach mainly relies on the performance of the algorithms as well as satellite image data [25].

Lineaments, which correspond to fractures, show the pathways of fluid flow processes [26, 27] such as groundwater and hydrothermal solutions [28]. Thus, lineament mapping is a crucial element in many geological studies, especially in mineral and hydrocarbon exploration [22, 29] as well as in hydrogeology [20]. Additionally, lineaments can be employed for structural analysis to understand and reconstruct the geological history of a region [28, 30].

Advances in computer hardware technology have largely supported the study of geological structures using remote sensing [31]. Nowadays, with the recent developments in the earth observation system by applying remote sensing, multiple data sources and techniques are used for lineament characterization [3, 22]. Thus, automatic methods have become more practical and less time-consuming compared to manual methods [27, 32]. As a result, remote sensing applications represent a new development in the discipline of applied geology [33].

The objective of this work is to evaluate the capacities of several generations of satellites (Landsat 8, ASTER, Sentinel 2 and Sentinel 1) to map lineaments by the automatic extraction method. This study is considered as the starting point for future field work such as mining and hydrological explorations, as well as infrastructure engineering. This work is the first of its kind in the study area and focuses on the quantitative analysis of lineaments. Additionally, lineaments trends were compared to global and regional tectonic movement trends to understand the geodynamic context of this region.

2. Geological Setting

The Variscan belt of Morocco constitutes the southern extension of the Variscan belt of Europe [34, 35]. In the Central Meseta, the major phase of the Variscan belt was characterized by Late Carboniferous deformations [36, 37]. Furthermore, the emplacement of granitoids of ages ranging from 320 Ma to 270 Ma has also been associated with this major phase, including Zaer granite [38], the subject of this study.

The granite massif of Zaer is located in the Western Moroccan Meseta [37, 39], about 75 km south of the city of Rabat and 100 km ESE of the city of Casablanca. The Zaer granitic pluton is one of the most important Variscan granitoids in the Central Zone of the Western Moroccan Meseta (Fig. 1). It is elliptical in shape with an area of more than 450 km² [42, 43] (Fig. 2). Structurally, the granite massif of Zaer appears within the Paleozoic fields of the Khouribga-Oulmes anticlinorium (Fig. 2b). It is mainly oriented NE-SW parallel to the major Variscan structures of the Meseta domain [45, 46].

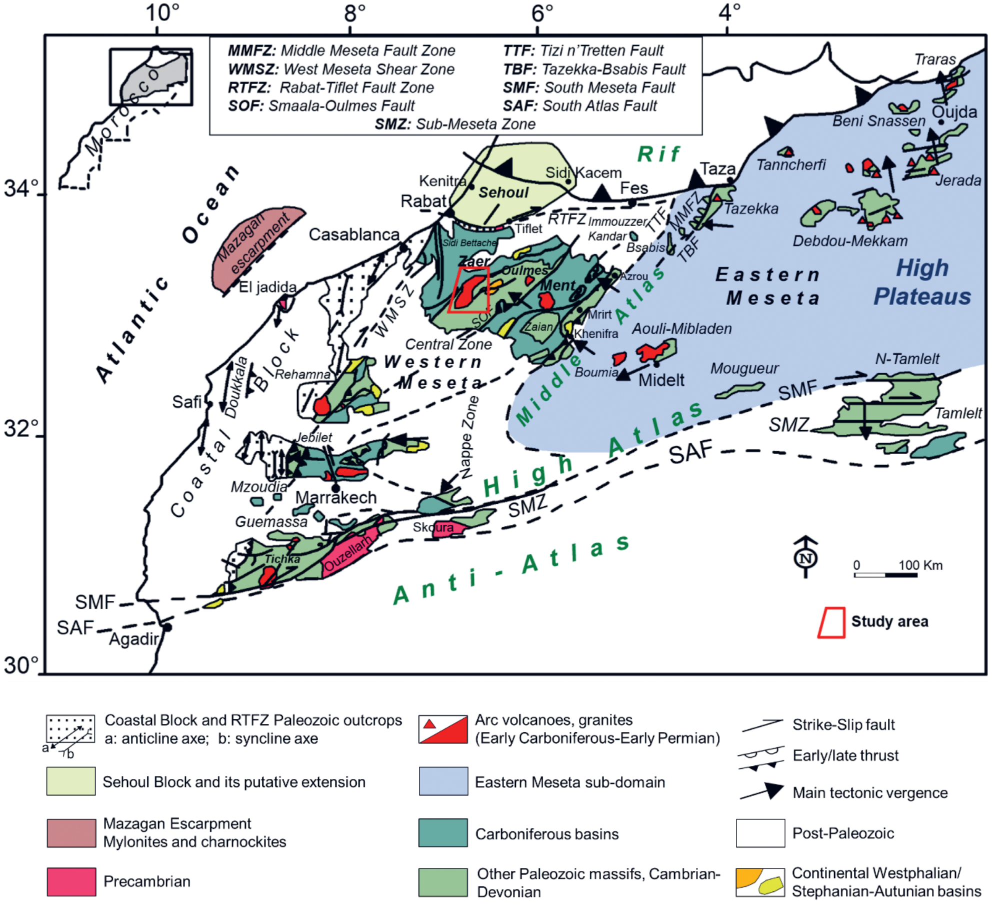

Fig. 1. Structural map of the Variscan domain of Meseta

Source: [40], modified after [41]

The host rocks of this granite massif are characterized by anchi- to epimetamorphic rocks. On the lithological level, the surrounding area is distinguished by the presence of Paleozoic formations including shales of Ordovician age to the east of the Zaer granite massif. As for the west of this massif, it is characterized by Upper Ordovician quartzites as well as Lower Devonian shales and limestones [37] (Fig. 2c). Paleozoic formations show an aureole of metamorphism around the Zaer granitic pluton, with a width of 1 km to 3 km [43, 47].

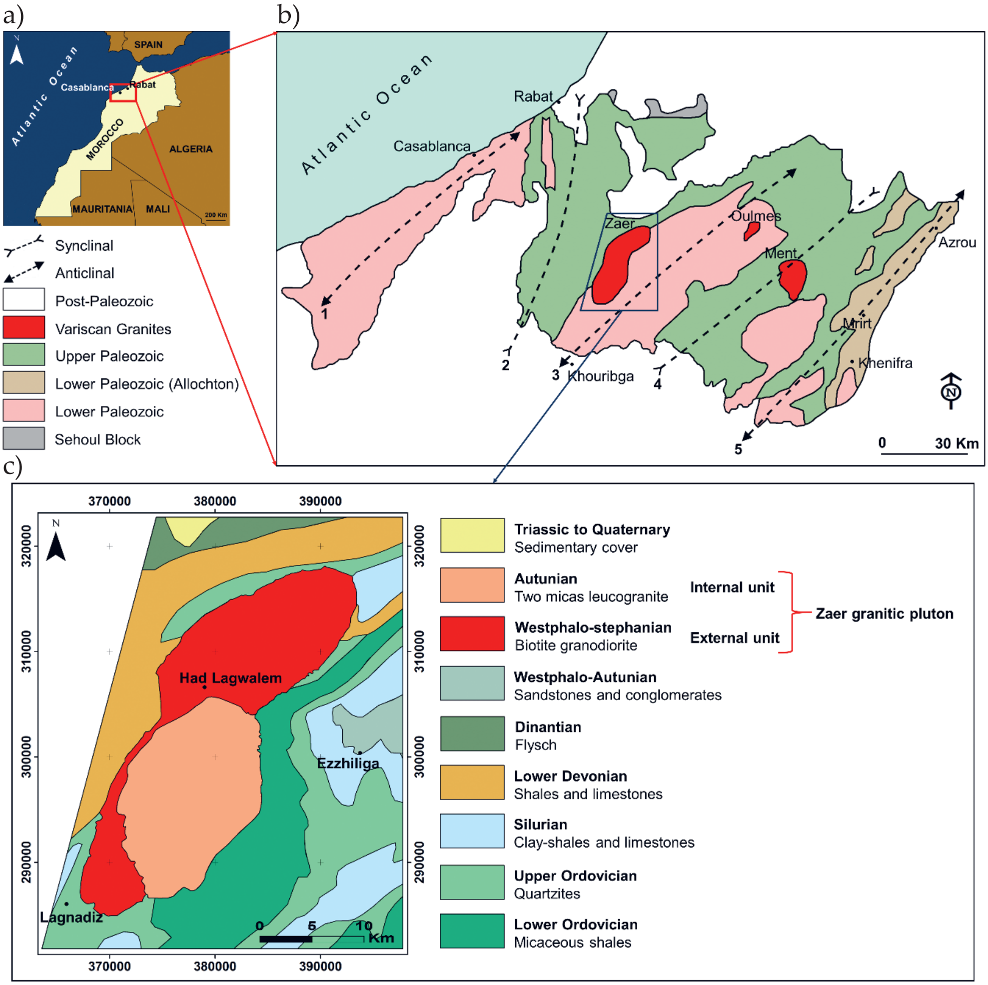

Fig. 2. Location of the study area on a national scale (a); different structural units of the Moroccan Variscan Massif (b): 1 – Casablanca anticlinorium, 2 – Western synclinorium, 3 – Khouribga-Oulmes anticlinorium, 4 – Fourhal-Telt synclinorium, 5 – Kasbat-Tadla-Azrou anticlinorium; lithologic map of the study area (c)

Source: fig. b [44], fig. c [37, 43, 47]

The Zaer granite massif consists essentially of two granite units [43, 47] (Fig. 2c): (i) the external unit occupies the northwestern and southern part of the granite formed mainly of biotite granodiorite and (ii) the internal unit formed by leucogranite with two micas. According to the radiometric ages (Rb-Sr) obtained on the main granite facies, the emplacement of the Zaer granite ranges between the Westphalo-Stephanian (303 Ma ±13 Ma) and the Autunian (279 Ma ±11 Ma) [38, 48].

3. Materials and Methods

3.1. Description of Data

Landsat 8 was released in 2013, is one of the latest generations of the Landsat series of satellites under the collaboration with the United States Geological Survey (USGS) and the National Aeronautics and Space Administration (NASA) [49, 50]. It carries two sensors: operational land imager (OLI) and thermal infrared sensor (TIRS). On the one hand, nine spectral bands define the OLI, including the visible (VIS), the near infrared (NIR), the short-wave infrared (SWIR) and the panchromatic band. On the other hand, the TIRS having two spectral bands, each characterized by 100 m in terms of spatial resolution (Table 1) [49, 51]. Landsat 8 OLI has been used in several works for lineament extraction [3, 26, 52].

Table 1. Characteristics of Landsat 8 and ASTER sensors

Landsat 8			ASTER			
Bands	Spectral range [μm]	Resolution [m]	Band number	Spectrometer	Spectral range [μm]	Resolution [m]
			1		0.52–0.60	
			2	VNIR	0.63–0.69	15
1. Coastal aerosol	0.43–0.45	30	3		0.78–0.86	
2. Blue	0.45–0.51	30	4		1.600–1.700	
3. Green	0.53–0.59	30	5		2.145–2.185	
4. Red	0.64–0.67	30	6		2.185–2.225	
5. NIR	0.85–0.88	30	7	SWIR	2.235–2.285	30
6. SWIR1	1.57–1.65	30	8		2.295–2.365	
7. SWIR2	2.11–2.29	30	9		2.360–2.430	
8. Panchromatic	0.50–0.68	15				
9. SWIR/Cirrus	1.36–1.38	30	10		8.125–8.475	
10. TIRS 1	10.60–11.19	100	11		8.475–8.825	
11. TIRS 2	11.50–12.51	100	12	TIR	8.925–9.275	90
			13		10.25–10.95	
			14		10.95–11.65	

The advanced spaceborne thermal emission and reflection radiometer, known as ASTER, is a multispectral image. The Ministry of Economy, Trade and Industry (METI) of Japan developed this multispectral sensor. Subsequently, NASA took over responsibility for its operation [53–55]. The Terra platform saw the launch of ASTER in December 1999 [56–58]. ASTER covers 14 bands including [53, 59–63]

(Table 1): (i) three bands in the visible and near infrared (VNIR) with a spatial resolution of 15 m; (ii) six bands in the short-wave infrared (SWIR) are characterized by a spatial resolution of 30 m, and (iii) five bands in the thermal infrared (TIRS) through a spatial resolution of 90 m. Additionally, geological mapping and mineral exploration have made extensive use of the ASTER sensor [2, 64–67].

The Copernicus space program includes the Sentinel satellites, which are operated by the European Space Agency (ESA) [68]. The latter has developed several satellite missions with different aspects of Earth observation [69]. Sentinel 2 and Sentinel 1 are two satellite images acquired respectively by the optical and SAR (synthetic aperture radar) systems [70]. In order to meet revisit and coverage requirements, each Sentinel mission relies on a constellation of two satellites [71]. June 2015 saw the launch of the Sentinel 2A sensor [72]. It contains 13 spectral bands using various spatial resolutions (10 m, 20 m and 60 m) [70, 73, 74]. The Sentinel 1A radar, which was launched in 2014, includes a C-band SAR instrument that offers various data acquisition modes. The main acquisition mode for land is called interferometric wide (IW) swath mode [75]. This mode allows the combination of a broad width of 250 km and a large spatial surface (5 × 20 m) [75]. Table 2 summarizes the characteristics of these satellites. Sentinel 2A and Sentinel 1A products have been widely used for several geological applications [76, 77], especially for mapping lineaments [21, 78].

Table 2. Characteristics of Sentinel 2A and Sentinel 1A sensors

Sentinel 2A			Sentinel 1A	
Bands	Spectral range [μm]	Resolution [m]		
1. Coastal aerosol	0.433–0.453	60	SAR frequency [GHz]	5.4
2. Blue	0.458–0.523	10		
3. Green	0.543–0.578	10	Imaging mode	IW
4. Red	0.650–0.680	10		
5. Red Edge 1	0.698–0.713	20	Swath [km]	250
6. Red Edge 2	0.733–0.748	20		
7. Red Edge 3	0.773–0.793	20	Resolution Gr × Az [m]	5 × 20
8. NIR	0.785–0.900	10		
8A. NIR narrow	0.855–0.875	20	Polarization	VV + VH
9. Water vapour	0.935–0.955	60		
10. SWIR/Cirrus	1.360–1.390	60	Data product	Ground Range Distance (GRD)
11. SWIR 1	1.566–1.655	20		
12. SWIR 2	2.100–2.280	20		

In order to confirm the accuracy of lineament extraction, this study was based on the shaded relief maps as well as the slope map. These maps are produced from the ASTER GDEM (global digital elevation model). The latter was extracted from the ASTER sensor. On June 29, 2009, GDEM was released jointly with NASA and METI, as part of the Global Earth Observing System contribution [79]. ASTER GDEM is the most recent digital topographic dataset, covering the global surface of the earth with 30 m in terms of spatial resolution [53]. Besides, ASTER GDEM has been widely used in many studies to verify geological lineaments [21, 80, 81]. In addition, this work also relied on the faults extracted from the geological maps (Ezzhiliga and Ait Ammar; 1:50,000), on the faults derived from the facies map of the Zaer pluton by [82] (1:20,000) and on the results of the field survey.

3.2. Pre-processing

The pre-processing step is important before the processing of optical and radar remote sensing images. The main pre-processing and processing steps are shown in the flowchart (Fig. 3).

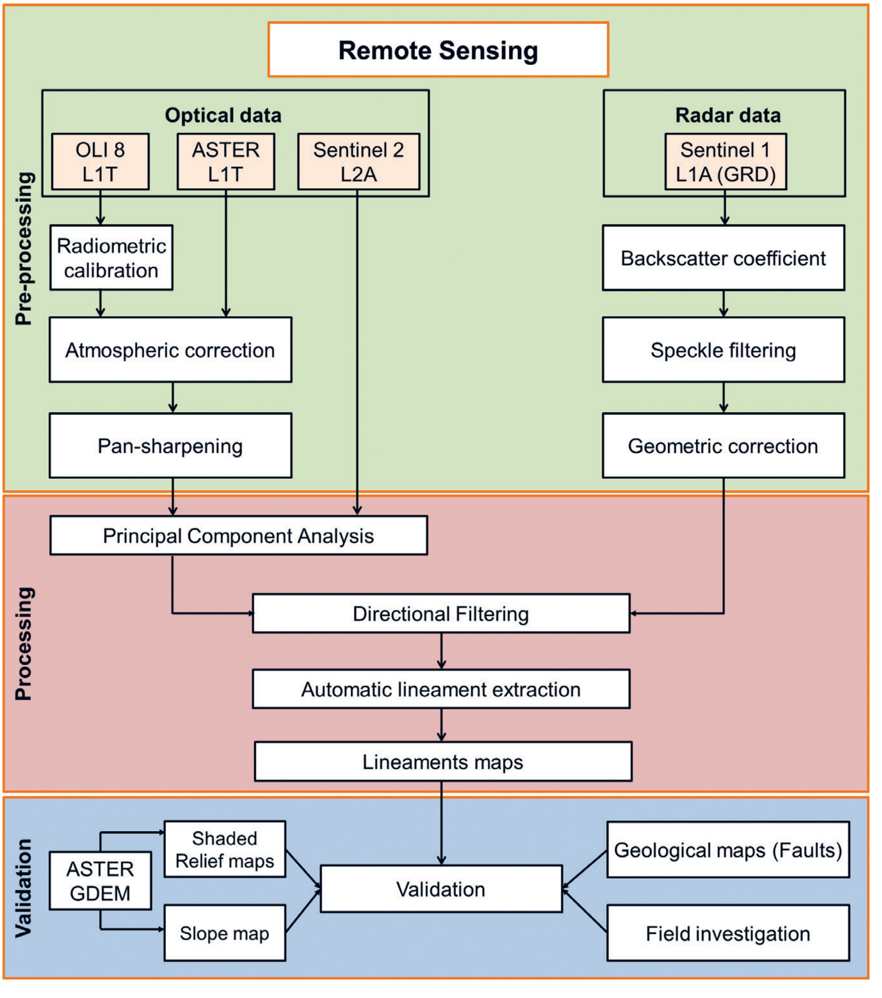

Fig. 3. Methodological flowchart of this study

The Landsat 8 image used corresponds to level 1T (corrected terrain), acquired on October 7, 2017. It is already geometrically corrected by applying the World Geodetic System 1984 (WGS84) datum and the Universal Transverse Mercator (UTM) projection [83]. The pre-processing step includes radiometric calibration and atmospheric correction. First, a radiometric calibration was applied in order to transform the digital numbers into values reflected by the surface. Afterward, the FLAASH (fast line-of-sight atmospheric analysis of spectral hypercubes) module was performed to correct the atmosphere [3, 84].

Concerning the ASTER image, obtained on November 8, 2005, at level 1T (precision terrain corrected registered at-sensor radiance). It comes with the WGS84 world datum and Universal Transverse Mercator (UTM). In addition, this level is also radiometrically calibrated [85]. Thereafter, with the same atmospheric correction method used in the Landsat data, the atmospheric correction was implemented using the FLAASH module [86].

The VNIR and SWIR bands of the OLI and ASTER images were resampled in this study with a spatial resolution of 15 m using the Gram–Schmidt pansharpening method. The panchromatic band of the OLI sensor was applied to generate data with a high spatial resolution of 15 m [87]. The Gram–Schmidt method invented by [88] has emerged as one of the most widely used algorithms for pansharpening of multispectral images [89]. It is based on merging a panchromatic image characterized by higher spatial resolution with a set of spectral bands with lower spatial resolution [88]. The Gram–Schmidt method is widely used in many remote sensing researches [90, 91].

For the Sentinel 2A image, acquired on July 5, 2020, distributed at level 2A (bottom of atmosphere corrected reflectance). These data have been radiometrically calibrated and geometrically corrected [92] using the same global datum and projection as the data from Landsat 8 and ASTER. Furthermore, this product is atmospherically corrected by the European Space Agency (ESA) [92–94]. Thereafter, a spatial resolution of 10 m was used to resample the spectral bands.

With regard to the Sentinel 1A radar image, it was obtained on July 14, 2018, at level 1 GRD (ground range detected). The pre-processing workflow consists of three steps. First, the radiometric calibration procedure was used to transform the digital pixel values into backscatter values reflected from the surface [90, 95]. Second, ''Lee'' speckle filtering was used to increase image quality by reducing speckle noise [12, 95]. Finally, with the use of the range Doppler terrain correction technique for the correction of the geolocation accuracy of the imagery and transformed into geographical coordinates (latitude/longitude, WGS84) [96] from the image of the Shuttle Radar Topography Mission (SRTM) with a spatial resolution of 90 m [68, 95]. After the pre-processing step, the spatial resolution of the Sentinel 1A image is 10 m.

In order to unify the same global geodetic system and the same projection of satellite images and geological maps. All satellite images were georeferenced using the Lambert conformal conic projection; North Morocco zone, adopted in Morocco (spheroid: Clarke 1880, datum: Merchich).

3.3. Processing

In this study, the processing step initially focused on the use of Sobel filters on the first Principal Component of the optical images and on the VH as well as VV polarizations of the radar image. Subsequently, the line module algorithm was applied to the filtered images in order to extract the geological lineaments.

Principal Component Analysis

Principal component analysis (PCA) is a statistical technique commonly employed in geological research [26, 97, 98], particularly for mineral exploration and geological mapping [90]. This technique consists of selecting uncorrelated linear combinations of variables [99, 100] in order to create new bands called principal components (PC) from the information contained in the spectral bands [91, 101], so that each component extracts successive linear combinations in decreasing order of variance [99, 100]. The first PCA band (Fig. 4) contains high data compared to the second band, and so on; because they include very little data, the latest PCA bands seem noisy [62, 102].

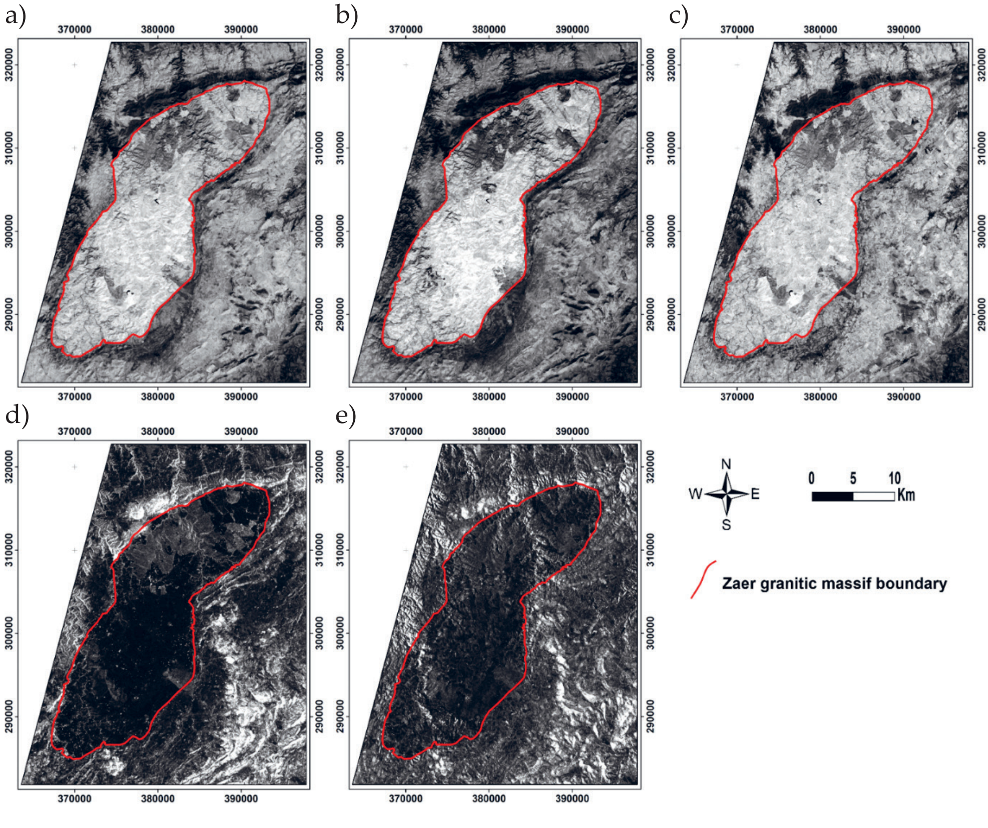

Fig. 4. PC1 of the OLI (a), ASTER (b), and Sentinel 2A (c) sensors, in addition to the VH (d) and VV (e) polarizations of the Sentinel 1A radar

Walsh and Mynar [103] evaluated the effectiveness of five different improvement techniques to identify lineaments which are the mean value of all bands, principal component analysis (PCA), band ratio (BR), histogram equalization and high-pass digital filtering. Based on this comparison, the results demonstrated that PCA is more effective for lineament mapping. PCA has been used in many studies for the determination of lineaments [28, 98, 104]. The directional filtering technique was applied to the PC1 extracted from each optical image. Generally, the PC1 was used because it contains the maximum of information and is characterized by a well-observed relief [9, 105].

Directional Filtering

Directional filtering is a technique that enhances the linear features that are to be identified in particular directions and edge enhancement in images [15, 52]. This technique is widely used to detect geological lineaments (faults and fractures) [106]. Therefore, the application of directional filters remains the best way to identify structural lineaments [21]. In this study, directional filters were used to apply to the first principal component as well as the VH and VV polarizations using the following four main directions: N-S, NE-SW, E-W and NW-SE with a 7 × 7 kernel matrix (Table 3). Figure 5 shows an example of directional filters derived from the VH polarization of the Sentinel 1A image.

Table 3. Four main directional filters with 7 × 7 kernel matrix

N-S							NE-SW						
1	1	1	2	1	1	1	0	1	1	1	1	1	2
1	1	2	3	2	1	1	−1	0	2	2	2	3	1
1	2	3	4	3	2	1	−1	−2	0	3	4	2	1
0	0	0	0	0	0	0	−1	−2	−3	0	3	2	1
−1	−2	−3	−4	−3	−2	−1	−1	−2	−4	−3	0	2	1
−1	−1	−2	−3	−2	−1	−1	−1	−3	−2	−2	−2	0	1
−1	−1	−1	−2	−1	−1	−1	−2	−1	−1	−1	−1	−1	0
E-W							NW-SE						
−1	−1	−1	0	1	1	1	2	1	1	1	1	1	0
−1	−1	−2	0	2	1	1	1	3	2	2	2	0	−1
−1	−2	−3	0	3	2	1	1	2	4	3	0	−2	−1
−2	−3	−4	0	4	3	2	1	2	3	0	−3	−2	−1
−1	−2	−3	0	3	2	1	1	2	0	−3	−4	−2	−1
−1	−1	−2	0	2	1	1	1	0	−2	−2	−2	−3	−1
−1	−1	−1	0	1	1	1	0	−1	−1	−1	−1	−1	−2

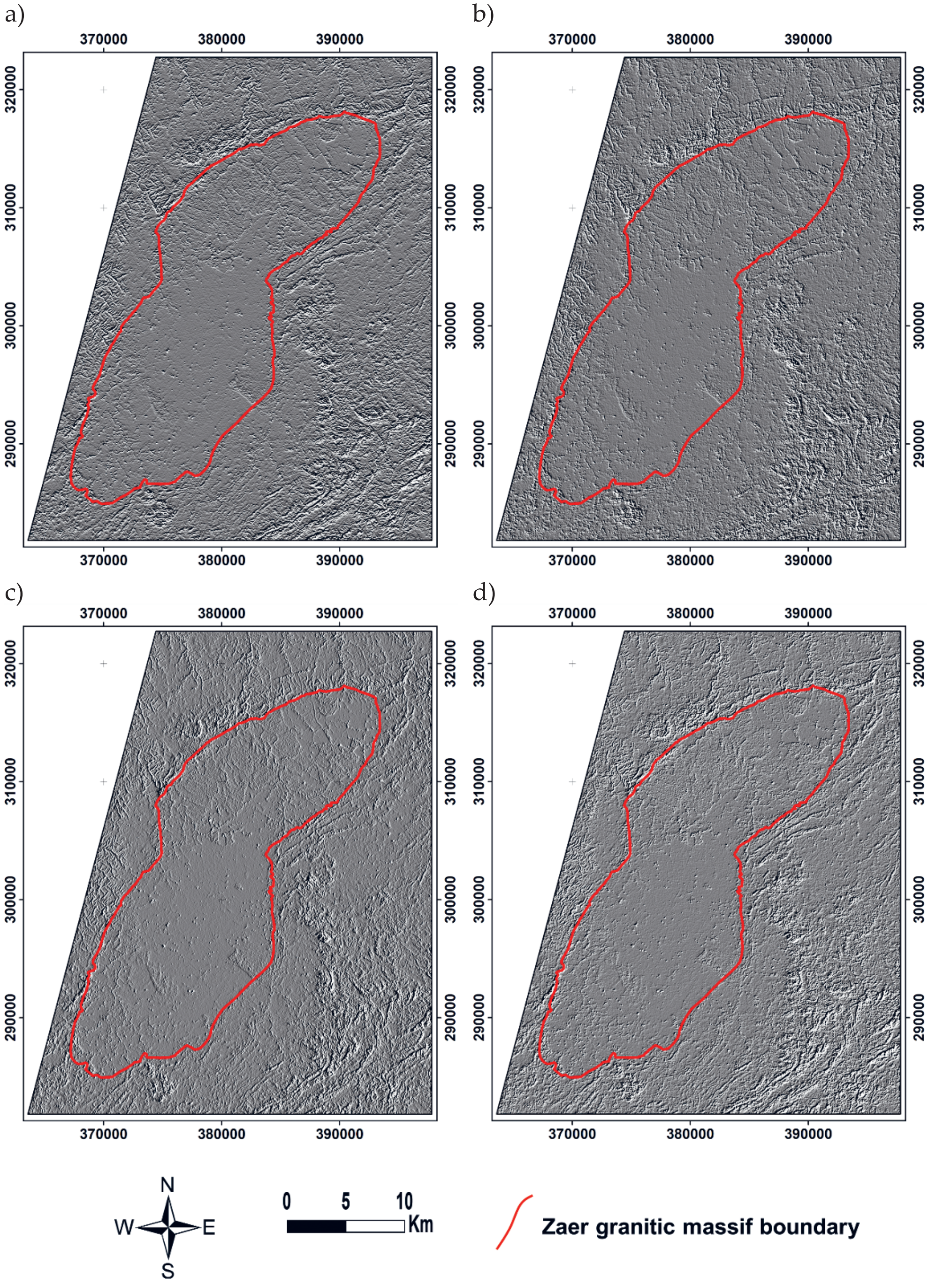

Fig. 5. Filtered images derived from the VH polarization of the Sentinel 1A sensor in the four main directions: a) N-S; b) NE-SW; c) E-W; d) NW-SE

Lineament Extraction

The automatic extraction in this study was carried out using the line module algorithm of the PCI Geomatica software. This algorithm consisted of two essential steps, namely edge detection followed by line detection, each step is characterized by a set of parameters [20, 80]. Table 4 describes these parameters in detail.

The automatic lineament extraction in this work was achieved by testing different parameters of optical and radar datasets. Table 5 represents the parameters used in the line module of the PCI Geomatica software to obtain the ideal parameters. These parameters were established taking into account the visual interpretation.

Table 4. Various parameters of the line module

Step	Parameter	Unit	Description
Edge detection	RADI (filter radius)	pixel	It specifies the radius of the filter applied for edge detection, whose values should be between 3 and 8, a higher value tends to include more noise
	GTHR (edge gradient threshold)	unitless	It defines the minimum threshold of the gradient level to detect contours. Values between 10 and 70 give good results
Line detection	LTHR (curve length threshold)	pixel	The minimum length of a curve that can be considered a lineament, values between 10 and 50 are desirable
	FTHR (line fitting threshold)	pixel	It indicates the biggest error that can occur when adjusting the line segment to create a lineament, ideal values range from 2 to 5
	ATHR (angular difference threshold)	degrees	It is used to specify the largest angle that can be formed between two lineaments to be joined. Values ranging from 3 to 20 are acceptable
	DTHR (linking distance threshold)	pixel	It presents the smallest distance necessary to connect two lineaments. 10 to 45 is a reasonable range for gradient values

Table 5. Values applied to line module parameters to automatically extract lineaments

Parameters	Applicable values
RADI	8
GTHR	50
LTHR	10
FTHR	3
ATHR	20
DTHR	20

4. Validation

Validation is one of the most significant steps in lineament extraction. To verify the results obtained from the study area, the extracted lineaments were first compared to the shaded relief maps and the slope map produced from the GDEM. In addition, these lineaments were compared to pre-existing faults in geological maps and also to field investigation.

4.1. Validation Using Shaded Relief Maps

Shaded relief maps are visual representations of the terrain [19, 107], derived from global digital elevation model (GDEM) data [108]. Thus, lineaments may exist where there are limits between shaded and unshaded zones [27]. A shaded relief map is produced by changing the virtual azimuth and elevation of the sun [19]. After a comparison of the different sun position angles, azimuths 0, 45, 90 and 135 were chosen because they are best exposed in shaded and unshaded areas [19]. It is characterized by an elevation angle of 45 degrees showing the altitude of the sun above the horizon [27].

4.2. Validation Using the Slope Map

The slope map is a product also derived from GDEM data [109, 110]. It is an important parameter which is widely used to validate the extraction of lineaments. In general, abrupt variations in slope values are frequently associated with the existence of linear structures [13, 111–114].

4.3. Validation Using Pre-existing Major Faults and Field Survey

In this work, a comparison of the extracted lineaments was made with the pre-existing major faults in the geological maps and the facies map of the Zaer pluton. In addition, several locations of structural lineaments in the work area were selected to validate the results obtained by the automatic lineament extraction.

5. Results and Discussion

Pre-processing of optical and radar images plays an important role in reducing errors associated with data acquisition, such as atmospheric and cloud cover effects, which improves the visibility of linear features during the processing step in order to obtain a more detailed mapping [115]. For the optical images, the extracted lineaments were carried out on the directional filters of Sobel applied on the first principal component for each sensor. For the radar image, lineament extraction was performed on Sobel directional filters applied directly to the VH and VV polarizations. Therefore, the automatic extraction procedure was applied with the PCI Geomatica software, using the line module algorithm. This algorithm depends on the detection of edge and line, which is characterized by its speed and reliability in the results obtained [116].

In recent years, shaded relief and slope maps have been considered a reference source for lineament validation. In addition, the lineaments obtained from the automatic extraction were superimposed on the shading and slope maps to check the correspondence with the illumination areas and abrupt changes in slope, respectively. Lineaments obtained from OLI, ASTER, and Sentinel 2A show much less correlation with shading and abrupt changes in slope. Generally, the lineaments are also found in the regions with no change in values (low values) (Figs. 6, 7).

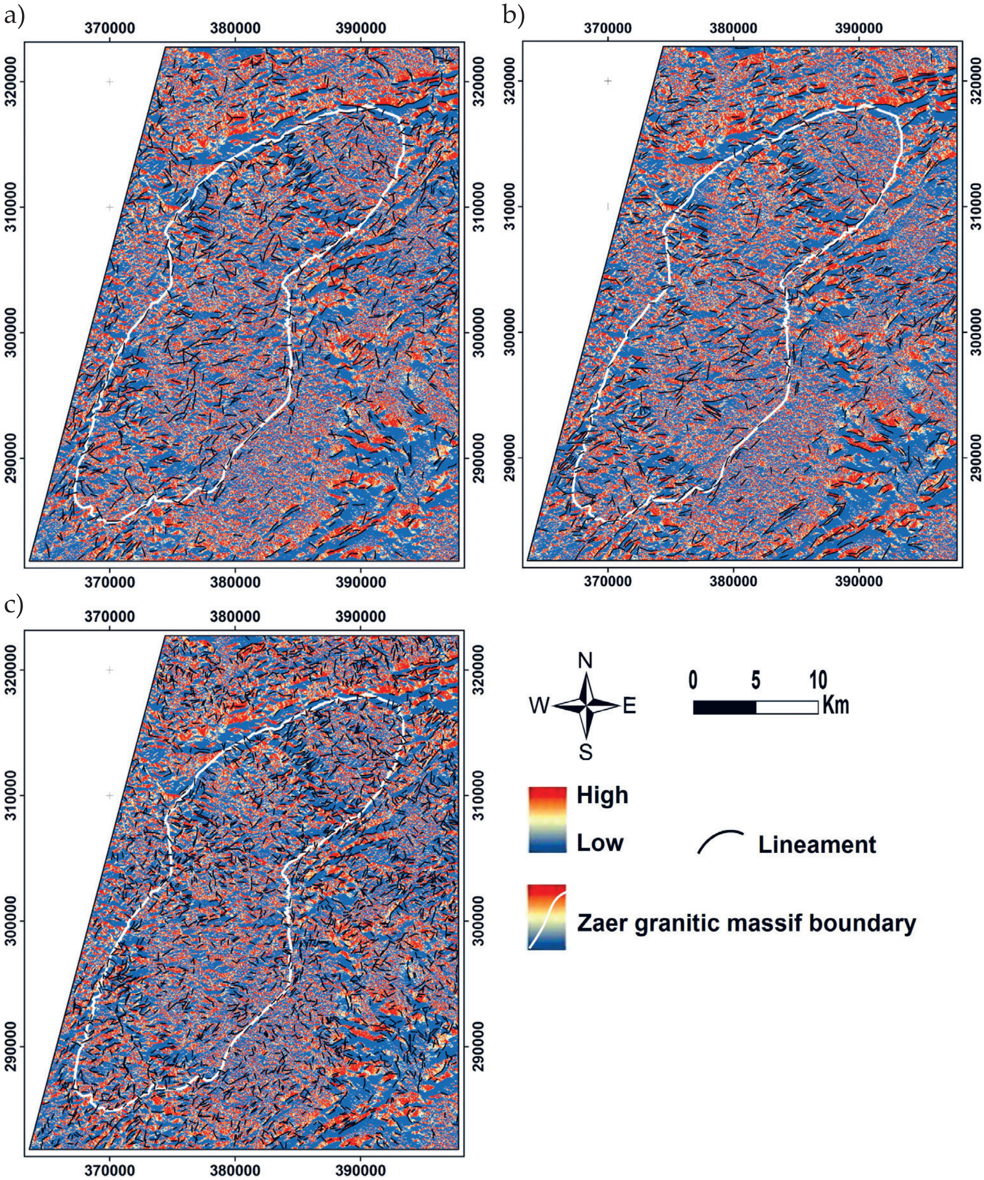

Fig. 6. Superposition of lineaments resulting from optical images OLI (a), ASTER (b), and Sentinel 2A (c) on the N0° shaded relief map

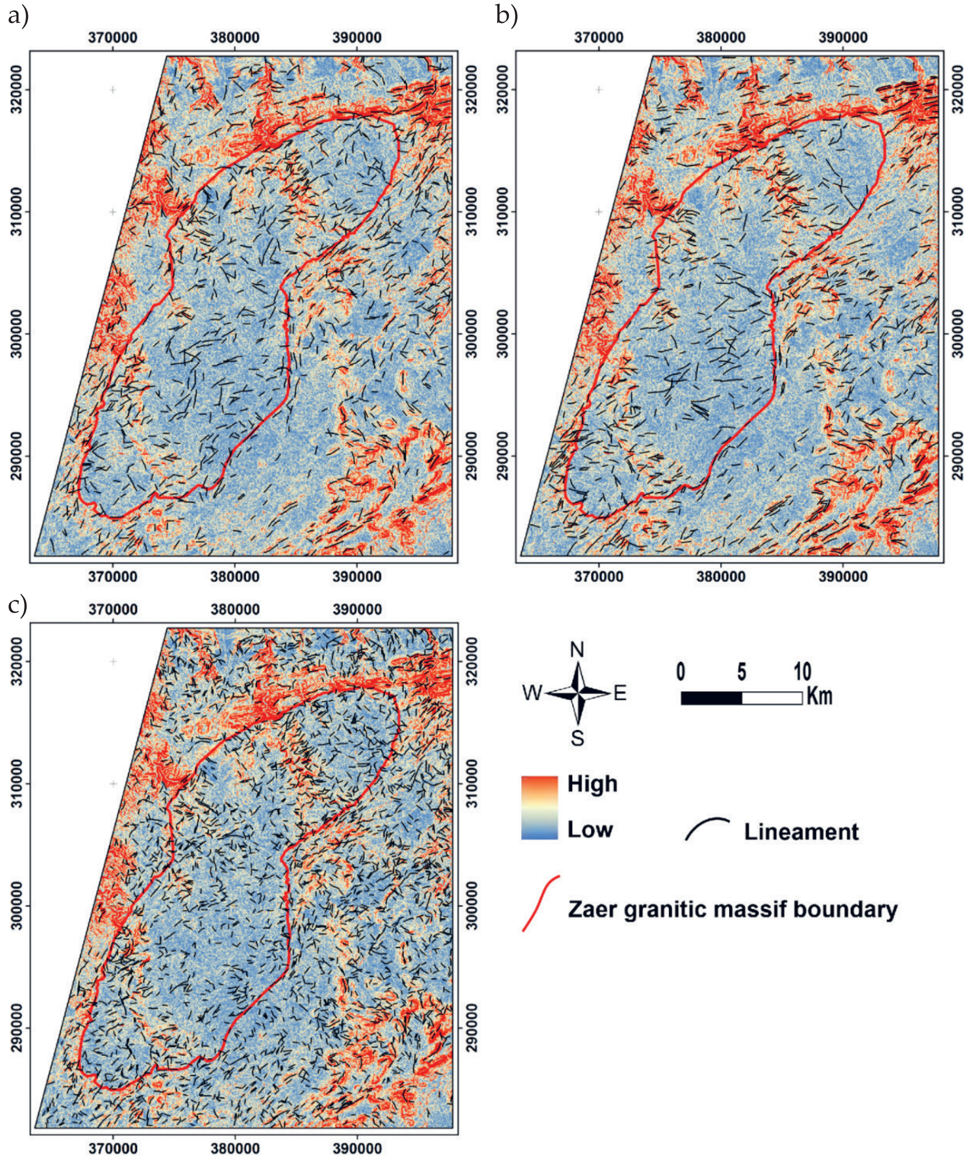

Fig. 7. Superposition of lineaments extracted from optical images OLI (a), ASTER (b), and Sentinel 2A (c) on the slope map

On the other hand, the results show that the majority of lineaments derived from the VH and VV polarizations are mainly found along the boundary of the shaded and unshaded areas (Fig. 8), as well as in the regions where the slope values change abruptly (Fig. 9). Thus, this explains why radar data is more sensitive to geomorphology than optical data [21, 80].

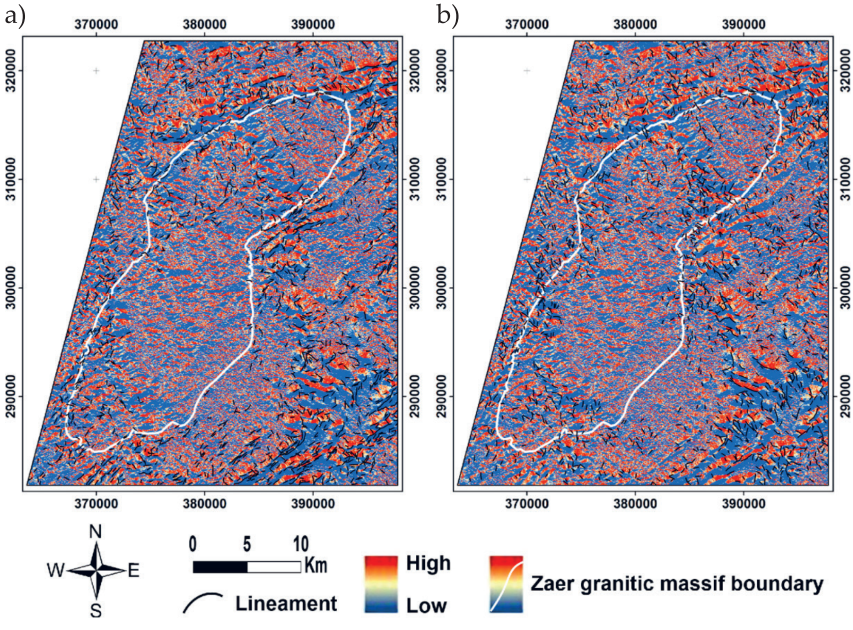

Fig. 8. Superposition of lineaments extracted from the VH (a) and VV (b) polarizations of Sentinel 1A on the N0° shaded relief map

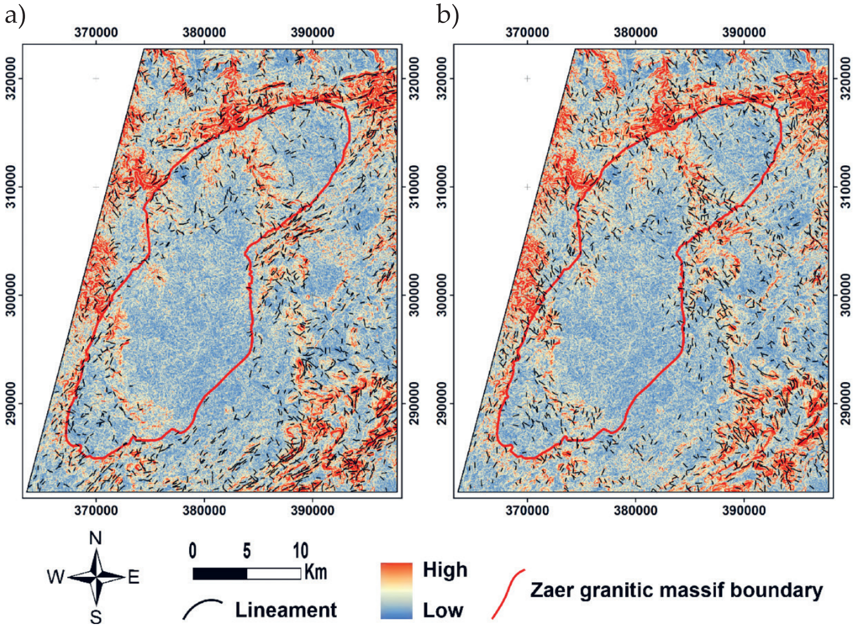

Fig. 9. Superposition of lineaments extracted from VH (a) and VV (b) polarizations (Sentinel 1A) on the slope map

In the present study, the superposition was used to analyze the distribution between the lineaments taken through the satellite imagery and the faults extracted from the geological maps related to the study area. The results of the analysis revealed that the concentration of lineaments in OLI, ASTER, and Sentinel 2A images are mostly randomly concentrated throughout the study area (Figs. 10, 12a–c).

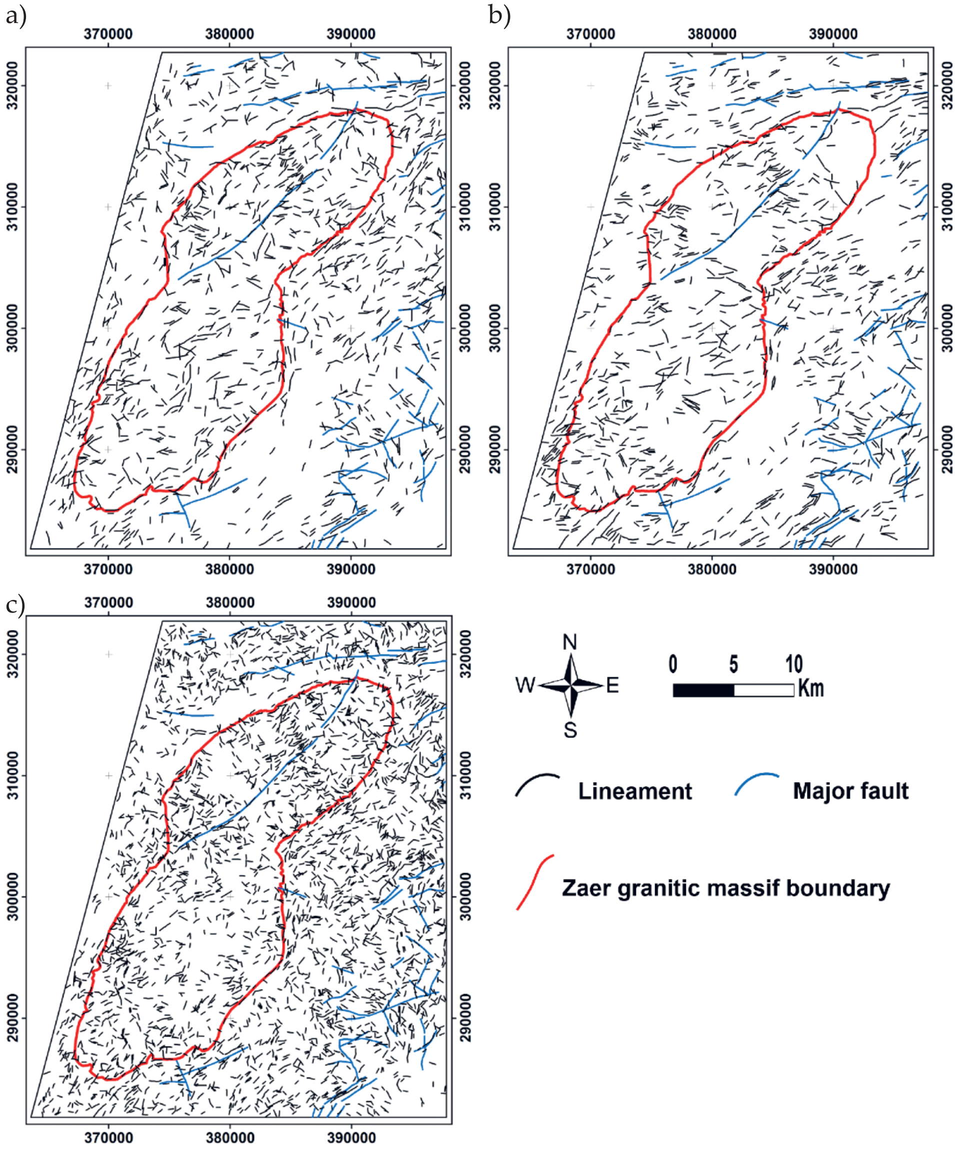

Fig. 10. Superposition of the lineaments obtained from the optical images of OLI (a), ASTER (b), and Sentinel 2A (c) on the major faults extracted from the geological maps (1:50,000)

In contrast, the lineaments derived from the VH and VV images indicate a good correlation with the faults (Figs. 11, 12d, e). Consequently, the radar image (VH and VV polarizations) gives more effective lineaments where there are steep slopes, shadow areas and rough terrain. Moreover, radar sensors depend essentially on the surface topography [117] which confirms the greater sensitivity of Sentinel 1 radar data to geomorphology than optical data.

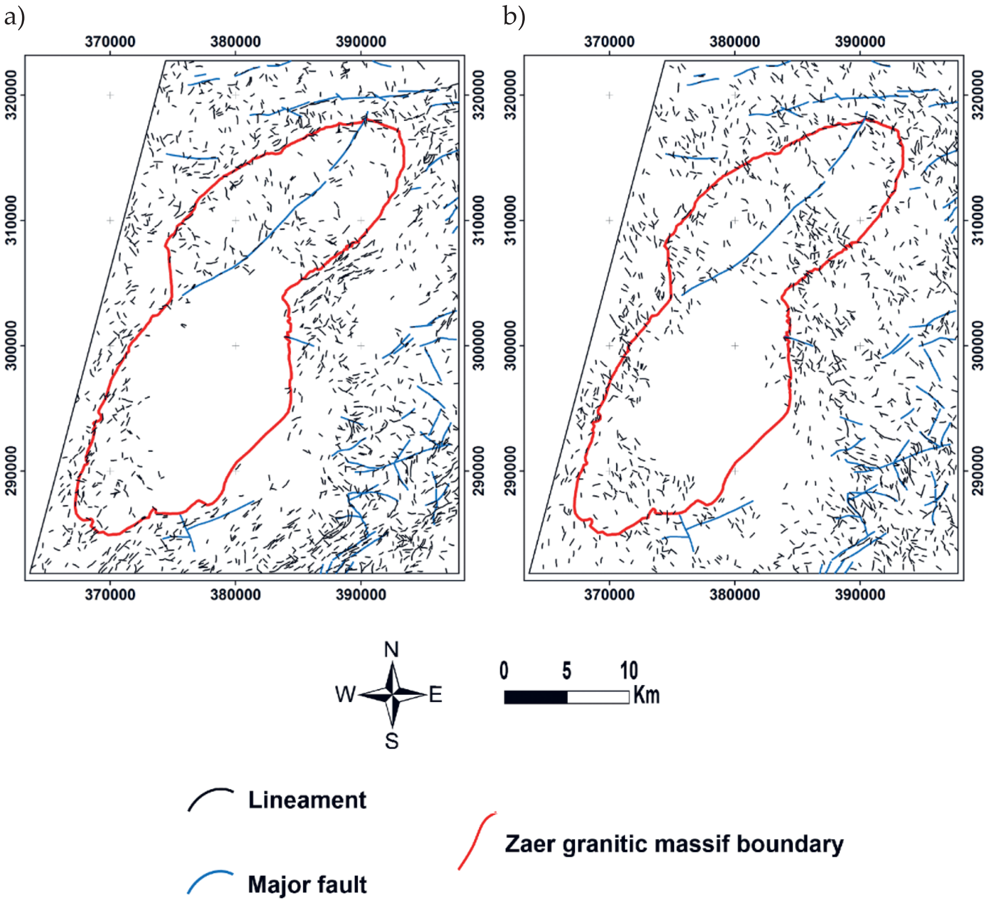

Fig. 11. Superposition of lineaments obtained by VH (a) and VV (b) polarizations (Sentinel 1A) on the major faults extracted from geological maps of the study area 1:50,000

The results obtained were used for structural analysis to understand the spatial distribution of lineaments in the working area. This task is based on three processes including length, density, and orientation. Moreover, these results can be used to compare the trends of the lineaments obtained from the VH and VV polarizations with the trends of the global and regional tectonic movements.

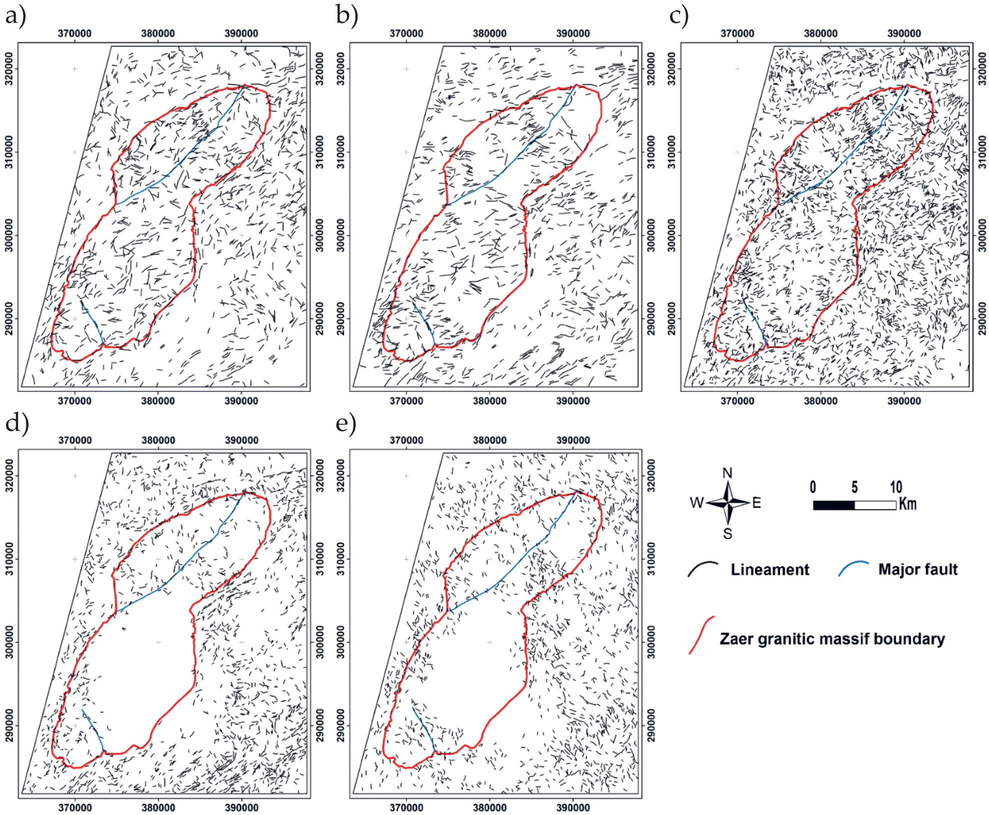

Fig. 12. Superposition of the lineaments obtained from the OLI (a), ASTER (b), and Sentinel 2A (c) images, in addition to the VH (d) and VV (e) polarizations on the major faults extracted from the facies map of the Zaer pluton (1:20,000)

5.1. Lineament Analysis

Lineament Length

Statistical lineament analysis (Fig. 13) showed that the numbers of lineaments resulting from the optical images are 2607, 2086 and 5997 of OLI, ASTER, and Sentinel 2A, respectively. Moreover, the VH and VV polarizations represent respectively 3177 and 2961 lineaments. Based on the length histograms, it can be noted that the most dominant lengths are between 200 m and 300 m for OLI and ASTER as well as between 100 m and 200 m for Sentinel 2A, VH and VV. Regarding the lineament values, the length varies between 30 m and 999 m for OLI. Also, the values associated with the ASTER image range from 30 m to 999 m. Values between 20 m and 982 m correspond to Sentinel 2A. The lengths of Sentinel 1A lineaments vary between 18 m and 944 m for VH and between 18 m and 995 m for VV. Moreover, the difference in results is explained by the distinct nature of each sensor.

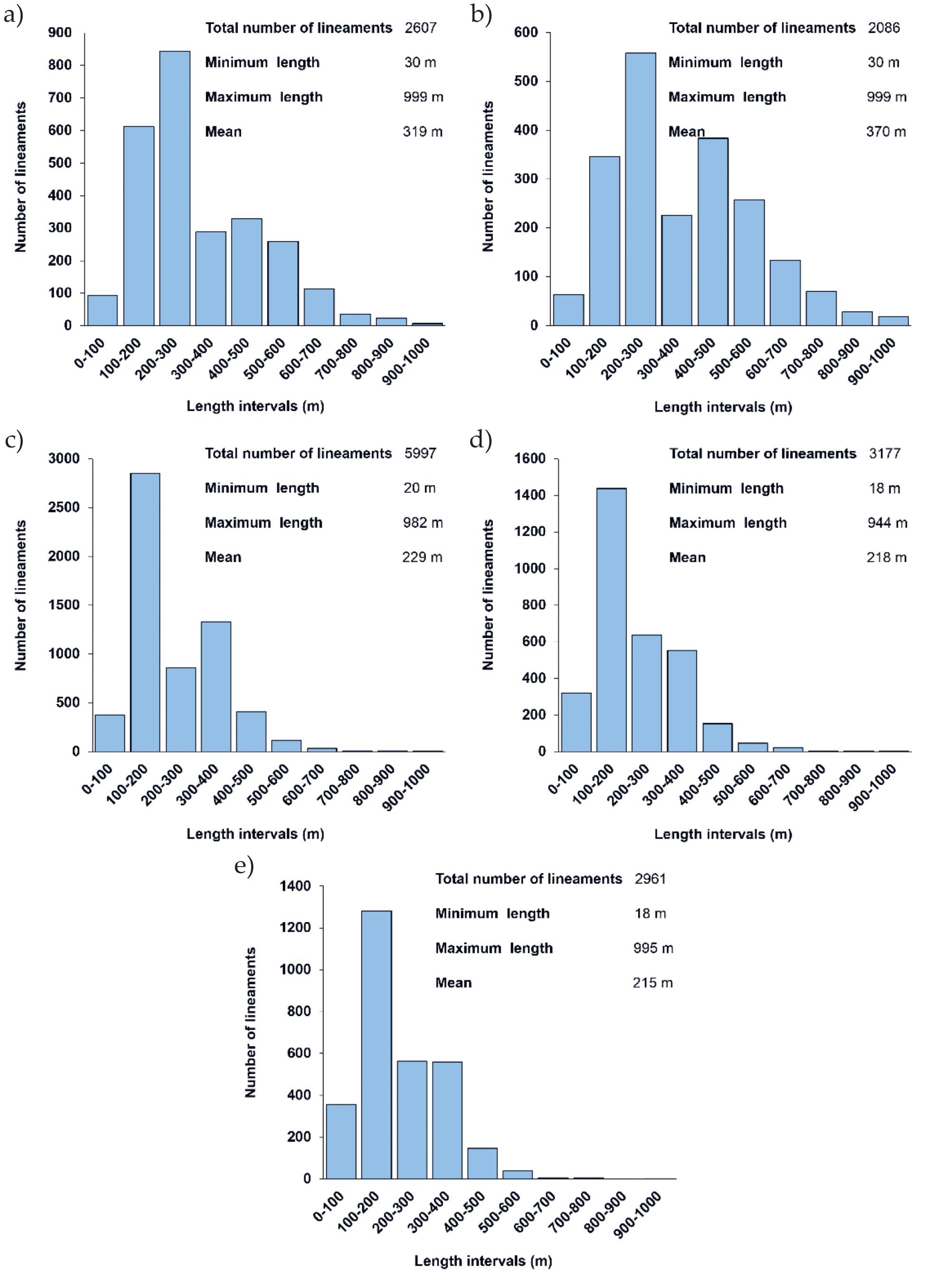

Fig. 13. Distribution histograms showing the number of lineaments as a function of length in the different satellite images of OLI (a), ASTER (b), and Sentinel 2A (c), in addition to VH (d) and VV (e) polarizations of Sentinel 1A

Lineament Density

Lineament density is an important tool widely used in spatial analysis [12, 118]. It is determined from the frequency of lineaments calculated per unit area (number of lineaments per square kilometer) [2, 20, 119]. In the study area, lineament density maps were produced to discover the correlation between the distribution of pre-existing faults and the concentration of lineaments. Concerning the Sentinel 1A sensor, the VH and VV images provide a dense network of lineaments in the zones associated with the faults, which are located in areas with significant geomorphology (Fig. 14d, e). Generally, the OLI, ASTER, and Sentinel 2A images show an abundance of lineaments in the granite and also in the surrounding area of the granite (Fig. 14a–c). Moreover, the high values of the optical images randomly cover most of the study area. The evaluation of the results obtained by different satellite images confirms that the Sentinel 1A radar data are the best correlated with pre-existing faults. This also proves the results obtained by the shaded relief maps and the slope map.

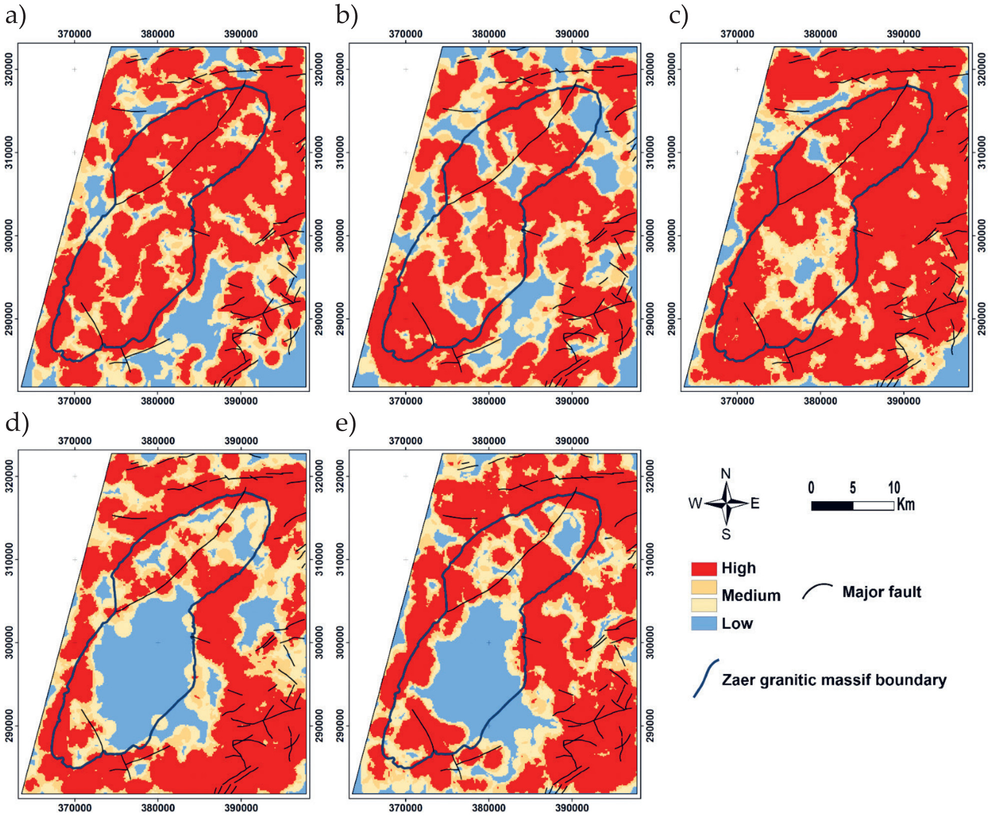

Fig. 14. Lineament density maps extracted from optical images of OLI (a), ASTER (b), and Sentinel 2A (c), in addition to VH (d) and VV (e) polarizations of Sentinel 1A

Lineament Orientation

The orientation of the lineament facilitates the determination of the main frequencies of the study area. Lineaments are usually grouped by an angular spacing of 10° [20]. The directions of the lineaments obtained can be compared to the directions related to existing faults in the studied area (Fig. 15). The resulting rose diagram indicates that the lineaments derived from the OLI and ASTER data presented a dominance of the NE-SW to ENE-WSW and E-W systems (Fig. 15a, b). Systems oriented N-S, NE-SW, E-W and NW-SE were well detected in the Sentinel 2A data (Fig. 15c). The main lineaments provided by the radar data are oriented NE-SW and NW-SE to NNW-SSE respectively for the VH and VV polarizations (Fig. 15d, e). Therefore, the orientations obtained by the radar image indicate a similarity with the orientations of the pre-existing faults (Fig. 15d–g).

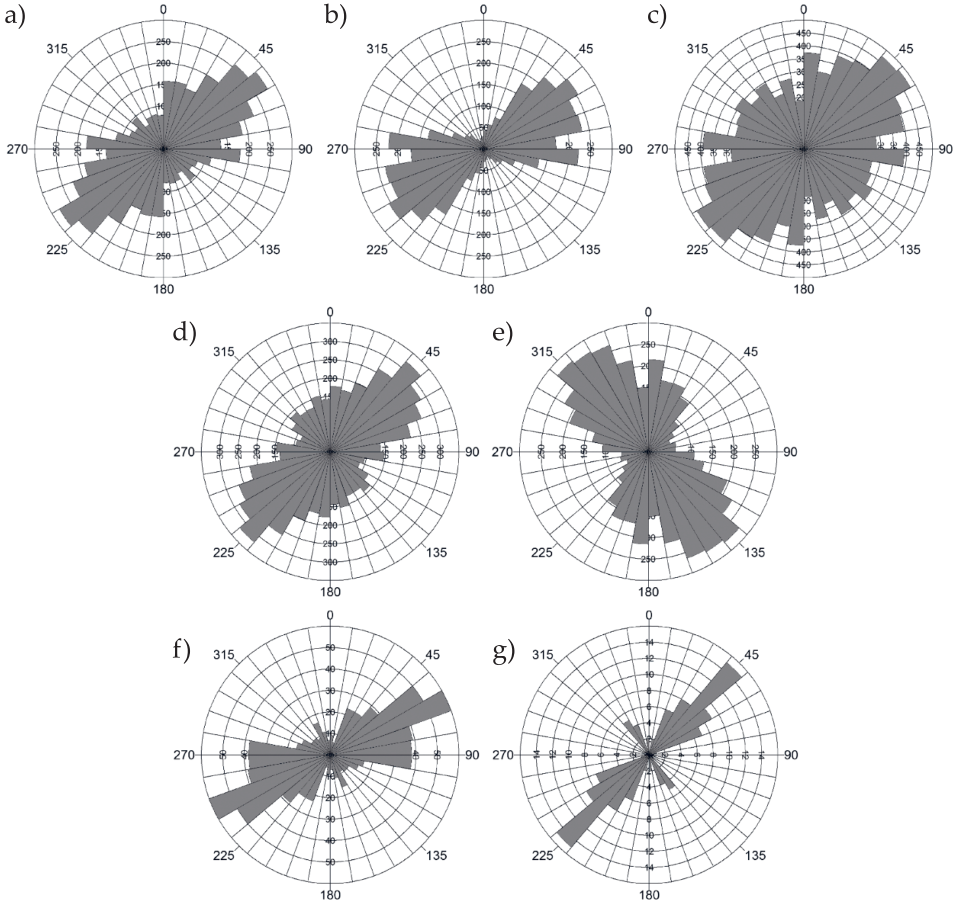

Fig. 15. Rose diagrams showing the main orientations of lineaments obtained from OLI (a), ASTER (b), Sentinel 2A (c), in addition to VH (d) and VV (e) polarizations; faults orientations extracted from the geological maps (1:50,000) (f) and from the facies map (1:20,000) (g) of the study area

5.2. Field Investigation

The results obtained through the various optical images (OLI, ASTER, and Sentinel 2A) as well as the radar data (VH and VV polarizations) indicate that the radar image is more accurate in the process of extracting of geological lineaments. Therefore, the combination of lineaments derived from the polarizations of VH and VV gives more accurate results (Fig. 16a). These interpretations relied on visual comparison of results with field investigation and existing data. In this study, several sites were chosen in the field for the validation of the results obtained from the radar image (VH and VV polarizations) (Fig. 16).

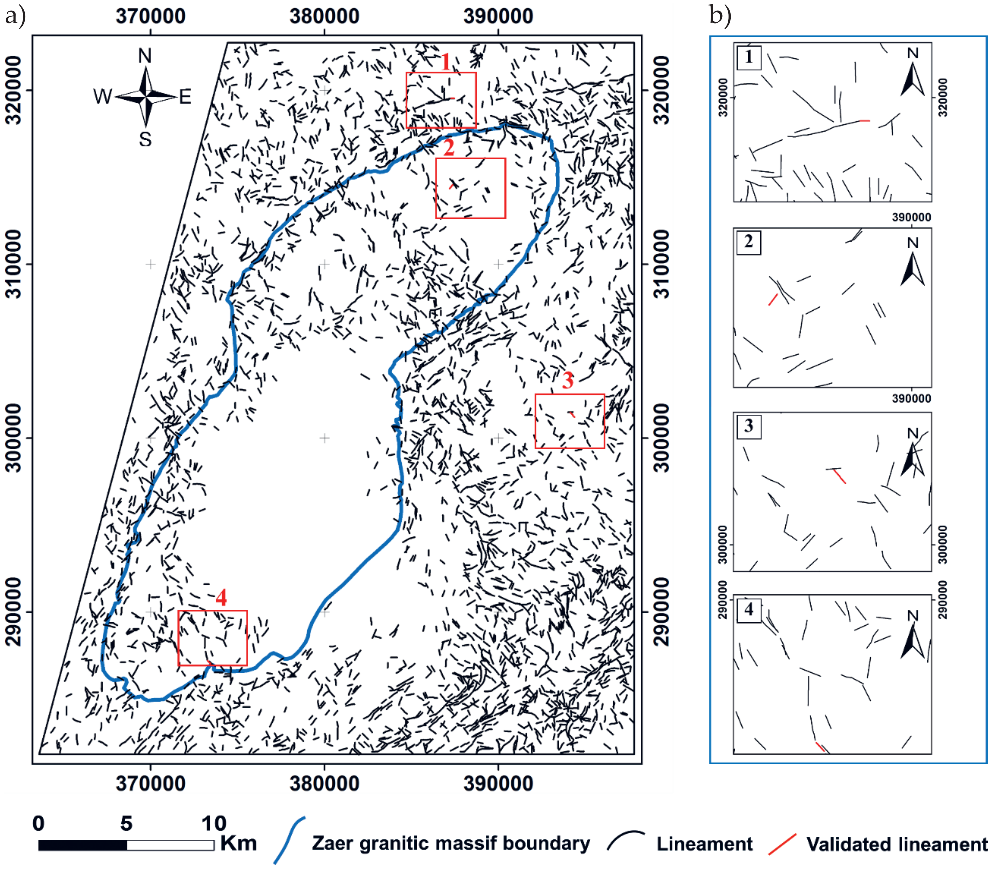

Fig. 16. Location of the field photographs on the lineament map obtained by the combination of the extracted lineaments of the VH and VV polarizations, with the extracted lineaments (in black) and the validated lineaments (in red) (a) and zoom on lineaments verified in the field (b)

Figure 17 provides a visual representation of the validated lineament observed in the field.

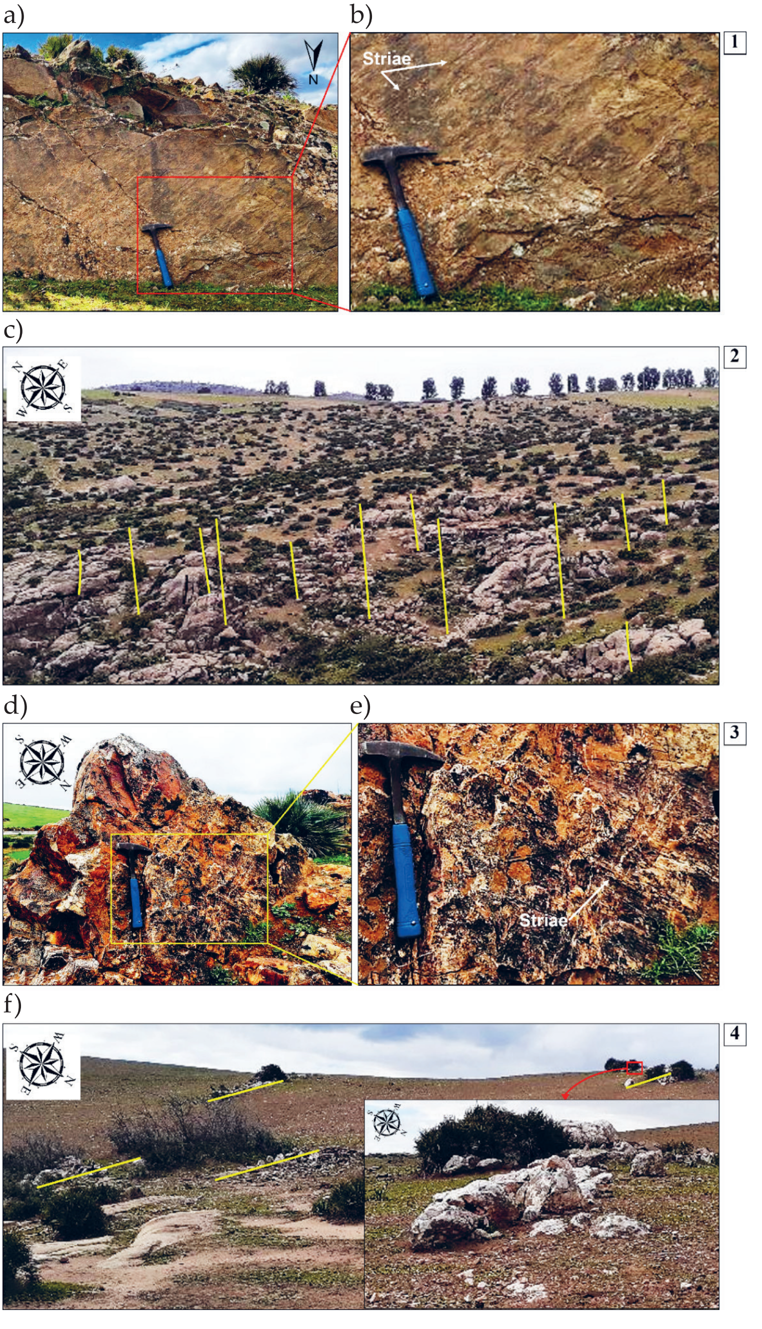

Fig. 17. Field photographs show some examples of lineament verified in the study area (see Figure 16 for location 1–4): E-W oriented fault (a) with striations in the fault mirror (b); sets of NE-SW oriented parallel faults in biotite granodiorite (c); NW-SE oriented fault (d) with slip faces (striations) (e); NW-SE oriented quartz veins (f)

Moreover, Figure 17 also shows the main aspects and characteristics of the lineament, helping in its overall understanding. The selection of these sites was mainly based on their accessibility. In addition, the field investigation strongly supports the other validation parameters (shaded relief maps, slope map and pre-existing faults). The faults in the working area are marked by the existence of striation on the fault surfaces. Striations are formed on fault surfaces by friction between two solids [120, 121]. These striations are considered a robust indicator for fault identification [122] as well as for determining fault slip direction [120, 123]. For the fractures examined in this study, it appears that most of them are oriented NE-SW and NW-SE with striations on fault surfaces in some places (Fig. 17).

5.3. Relationship between Lineament Directions and Tectonic Movement Directions

In Morocco, Variscan deformation began in the Late Devonian and continued until the Late Carboniferous. In general, three main phases have been distinguished in the realization of the Variscan deformation [36]: (i) the Late Devonian phase or Eovariscan phase, well developed in the eastern areas of the Moroccan Meseta and in the allochthonous alpine domains of the Rif; (ii) the Visean phase restricted to the boundary between the east and west of the Moroccan Meseta. Therefore, the two previous phases of compression were contemporaneous with the development of transtensive sedimentary basins that extended between the Late Devonian and the Early Carboniferous and (iii) the Late Carboniferous phase, during this period the entire Variscan domain, which includes the Western Moroccan Meseta and the Anti-Atlas, was affected by regional shortening.

According to the results obtained from the final lineament map, the Zaer massif and its surroundings mainly present two fracture systems oriented NE-SW and NW-SE to NNW-SSE. Furthermore, the Late Carboniferous deformation field of the Western Moroccan Meseta plutons, including the Zaer granitic pluton, is distinguished by a NW-SE shortening and a NE-SW horizontal stretching associated with the movement of strike-slips oriented essentially dextral ENE [124, 125]. This deformation field is part of the global tectonic regime associated with continental convergence movement. In addition, this era was marked by the westward displacement of Africa during the Late Carboniferous [124, 126].

The granite massif of Zaer presents a distribution parallel to the NE-SW faults. It is similar to the distribution of other Late Carboniferous granitic plutons from Western Moroccan Meseta, which indicate alignments parallel to NE-SW and ENE-WSW faults. These faults correspond to those inherited from the Proterozoic basement. Subsequently, these faults were reactivated during the Variscan orogeny [125, 127]. The NW-SE to NNW-SSE system is well expressed in different parts of central Morocco, including the Zaer granite and its surroundings. This direction is related to the replays of the submeridian faults of the Precambrian basement [128, 129].

6. Conclusion

The objective of this work was to compare the datasets of the optical sensors of Landsat 8, ASTER, Sentinel 2 as well as the radar sensor of Sentinel 1 in the automatic extraction of lineaments. The Sentinel 1 sensor gives greater accuracy than optical sensors, according to a comparison of the results obtained which included the shaded relief maps, the slope map, the correlation with the pre-existing faults in the geological maps as well as the field survey. The performance of radar data can be attributed to the high sensitivity of geomorphology compared to optical data which is affected by soil occupation. The methodology adopted generally depends on the availability of a set of techniques (principal component analysis and directional spatial filters) that have been applied to improve the image quality for automatic lineament extraction and analysis. Thus, the methodological approach used in the present study showed high efficiency in automatic lineament extraction, which can be applied quickly and inexpensively to extract geological lineaments in other similar areas. Lineament mapping is an important part of any structural geological study. In automatic lineament extraction, the accuracy and quality of the extracted lineaments not only depend on the input parameters of the PCI software, but also on the resolution of the satellite images. Therefore, the resolution of satellite images can have a strong influence on the accuracy and reliability of the extracted lineaments. Moreover, the results of this study confirm that the radar image will be very useful in mining and hydrogeological exploration.

Declaration of Competing Interest

The authors certify that they have no known competing financial interests or personal relationships that could have appeared to influence the work reported in this article.

Acknowledgements

The authors would like to thank the editors and anonymous reviewers for their valuable comments and constructive suggestions for this article. The Faculty of Sciences Ben M'sick, Hassan II University of Casablanca provided logistical support for the fieldwork.

References

[1] Hobbs W.H.: *Lineaments of the Atlantic border region*. Geological Society of America Bulletin, vol. 15(1), 1904, pp. 483–506. https://doi.org/10.1130/GSAB-15-483.

[2] Hung L.Q., Batelaan O., De Smedt F.: *Lineament extraction and analysis, comparison of LANDSAT ETM and ASTER imagery. Case study: Suoimuoi tropical karst catchment, Vietnam.* [in:] Ehlers M., Michel U. (eds.), *Remote Sensing for Environmental Monitoring, GIS Applications, and Geology V,* Proceedings of SPIE, vol. 5983, 2005, pp. 59830T1–59830T12. https://doi.org/10.1117/12.627699.

[3] Nath B., Niu Z., Acharjee S.: *Pre-earthquake anomaly detection and assessment through lineament changes observation using multi-temporal Landsat 8-OLI imageries: Case of Gorkha and Imphal.* Multi-purposeful Application of Geospatial Data, vol. 8, 2017, pp. 149–171. https://doi.org/10.5772/intechopen.72735.

[4] Zhumabek Z., Assylkhan B., Alexandr F., Dinara T., Altynay K.: *Automated lineament analysis to assess the geodynamic activity areas.* Procedia Computer Science, vol. 121, 2017, pp. 699–706. https://doi.org/10.1016/j.procs.2017.11.091.

[5] El-Sawy E.S.K., Ibrahim A.M., El-Bastawesy M.A., El-Saud W.A.: *Automated, manual lineaments extraction and geospatial analysis for Cairo-Suez district (Northeastern Cairo-Egypt), using remote sensing and GIS.* International Journal of Innovative Science, Engineering and Technology, vol. 3(5), 2016, pp. 491–500.

[6] Kocal A., Duzgun H.S., Karpuz C.: *Discontinuity mapping with automatic lineament extraction from high resolution satellite imagery.* ISPRS Archives [XXth ISPRS Congress Technical Commission VII, July 12–23, 2004, Istanbul, Turkey], vol. XXXV-B7, 2004, pp. 1073–1078.

[7] O'Leary D.W., Friedman J.D., Pohn H.A.: *Lineament, linear, lineation: Some proposed new standards for old terms.* Geological Society of America Bulletin, vol. 87(10), 1976, pp. 1463–1469. https://doi.org/10.1130/0016-7606(1976)87<1463:LLLSPN>2.0.CO;2.

[8] Souei A., Zouaghi T., Khemiri S.: *Lineament characterization for groundwater targeting using satellite images and field data.* Earth Science Informatics, vol. 16, 2023, pp. 455–479. https://doi.org/10.1007/s12145-022-00888-3.

[9] Zouaghi T., Harbi H.: *Airborne geophysics and remote sensing of an Nimas-Khadra area, southern Arabian shield: New insights into structural framework and mineral occurrences.* Advances in Space Research, vol. 70(11), 2022, pp. 3649–3673. https://doi.org/10.1016/j.asr.2022.08.046.

[10] Kassou A., Essahlaoui A., Aissa M.: *Extraction of structural lineaments from satellite images Landsat 7 ETM+ of Tighza Mining District (Central Morocco).* Research Journal of Earth Sciences, vol. 4(2), 2012, pp. 44–48.

[11] Ranganai R.T., Ebinger C.J.: *Aeromagnetic and Landsat TM structural interpretation for identifying regional groundwater exploration targets, south-central Zimbabwe Craton.* Journal of Applied Geophysics, vol. 65(2), 2008, pp. 73–83. https://doi.org/10.1016/j.jappgeo.2008.05.009.

[12] Corgne S., Magagi R., Yergeau M., Sylla D.: *An integrated approach to hydrogeological lineament mapping of a semi-arid region of West Africa using Radarsat-1 and GIS.* Remote Sensing of Environment, vol. 114(9), 2010, pp. 1863–1875. https://doi.org/10.1016/j.rse.2010.03.004.

[13] Jordan G., Schott B.: *Application of wavelet analysis to the study of spatial pattern of morphotectonic lineaments in digital terrain models. A case study.* Remote Sensing of Environment, vol. 94(1), 2005, pp. 31–38. https://doi.org/10.1016/j.rse.2004.08.013.

[14] Marghany M., Hashim M.: *Lineament mapping using multispectral remote sensing satellite data.* International Journal of the Physical Sciences, vol. 5(10), 2010, pp. 1501–1507.

[15] Pour A.B., Hashim M., Makoundi C., Zaw K.: *Structural mapping of the Bentong-Raub Suture Zone using PALSAR remote sensing data, Peninsular Malaysia: Implications for sediment-hosted/orogenic gold mineral systems exploration.* Resource Geology, vol. 66(4), 2016, pp. 368–385. https://doi.org/10.1111/rge.12105.

[16] Raj K.G.: *Origin and significance of Hem Avathi – Tirthahalli mega-lineament – A concept.* [in:] *IGARSS 89: 12th Canadian Symposium on Remote Sensing: Remote Sensing: An Economic Tool for the Nineties: Vancouver, Canada, July 10–14, 1989. Volume 1*, IEEE, Piscataway 1989, pp. 112–115. https://doi.org/10.1109/IGARSS.1989.567170.

[17] Jordan G., Meijninger B.M.L., van Hinsbergen D.J.J., Meulenkamp J.E., van Dijk P.M.: *Extraction of morphotectonic features from DEMs: Development and applications for study areas in Hungary and NW Greece.* International Journal of Applied Earth Observation and Geoinformation, vol. 7(3), 2005, pp. 163–182. https://doi.org/10.1016/j.jag.2005.03.003.

[18] Lim C.S., Komoo I., Tjia H.D.: *TiungSAT-1 imaging applications*. [in:] Othman M., Arshad A.S. (eds.), *TiungSAT-1: From Inception to Inauguration*, Astronautic Technology (M) Sdn. Bhd., Kuala Lumpur 2001, pp. 169–184.

[19] Abdullah A., Mat Akhir J., Abdullah I.: *Automatic mapping of lineaments using shaded relief images derived from digital elevation model (DEMs) in the Maran–Sungi Lembing area, Malaysia.* Electronic Journal of Geotechnical Engineering, vol. 15(J), 2010, pp. 949–957.

[20] Hashim M., Ahmad S., Md Johari M.A., Pour A.B.: *Automatic lineament extraction in a heavily vegetated region using Landsat Enhanced Thematic Mapper (ETM+) imagery.* Advances in Space Research, vol. 51(5), 2013, pp. 874–890. https://doi.org/10.1016/j.asr.2012.10.004.

[21] Javhar A., Chen X., Bao A., Jamshed A., Yunus M., Jovid A., Latipa T.: *Comparison of multi-resolution optical Landsat-8, Sentinel-2 and radar Sentinel-1 data for automatic lineament extraction: A case study of Alichur area, SE Pamir.* Remote Sensing, vol. 11(7), 2019, 778. https://doi.org/10.3390/rs11070778.

[22] Masoud A., Koike K.: *Auto-detection and integration of tectonically significant lineaments from SRTM DEM and remotely-sensed geophysical data.* ISPRS Journal of Photogrammetry and Remote Sensing, vol. 66(6), 2011, pp. 818–832. https://doi.org/10.1016/j.isprsjprs.2011.08.003.

[23] Raj S.K., Ahmed S.A.: *Lineament extraction from Southern Chitradurga Schist Belt using Landsat TM, ASTER GDEM and geomatics techniques.* International Journal of Computer Applications, vol. 93(12), 2014, pp. 12–20. https://doi.org/10.5120/16266-5993.

[24] Saadi N.M., Abdel Zaher M., El-Baz F., Watanabe K.: *Integrated remote sensing data utilization for investigating structural and tectonic history of the Ghadames*

Basin, Libya. International Journal of Applied Earth Observation and Geoinformation, vol. 13(5), 2011, pp. 778–791. https://doi.org/10.1016/j.jag.2011.05.016.

[25] Al-Dossary S., Marfurt K.J.: *Lineament-preserving filtering.* Geophysics, vol. 72(1), 2007, pp. P1–P8. https://doi.org/10.1190/1.2387138.

[26] Hamdani N., Baali A.: *Fracture network mapping using Landsat 8 OLI data and linkage with the karst system: A case study of the Moroccan central Middle Atlas.* Remote Sensing in Earth Systems Sciences, vol. 2(1), 2019, pp. 1–17. https://doi.org/10.1007/s41976-019-0011-y.

[27] Masoud A., Koike K.: *Tectonic architecture through Landsat-7 ETM+/SRTM DEM-derived lineaments and relationship to the hydrogeologic setting in Siwa region, NW Egypt.* Journal of African Earth Sciences, vol. 45(4–5), 2006, pp. 467–477. https://doi.org/10.1016/j.jafrearsci.2006.04.005.

[28] Si Mhamdi H., Raji M., Maimouni S., Oukassou M.: *Fractures network mapping using remote sensing in the Paleozoic massif of Tichka (Western High Atlas, Morocco).* Arabian Journal of Geosciences, vol. 10(5), 2017, 125. https://doi.org/10.1007/s12517-017-2912-5.

[29] Pour A.B., Hashim M.: *ASTER, ALI and Hyperion sensors data for lithological mapping and ore minerals exploration*. SpringerPlus, vol. 3, 2014, 130. https://doi.org/10.1186/2193-1801-3-130.

[30] Aydogan D., Pinar A., Elmas A., Tarhan Bal O., Yuksel S.: *Imaging of subsurface lineaments in the southwestern part of the Thrace Basin from gravity data.* Earth Planets Space, vol. 65(4), 2013, pp. 299–309. https://doi.org/10.5047/eps.2012.08.014.

[31] Xu J., Wen X., Zhang H., Luo D., Li J., Xu L., Yu M.: *Automatic extraction of lineaments based on wavelet edge detection and aided tracking by hillshade*. Advances in Space Research, vol. 65(1), 2020, pp. 506–517. https://doi.org/10.1016/j.asr.2019.09.045.

[32] Yeomans C.M., Middleton M., Shail R.K., Grebby S., Lusty P.A.J.: *Integrated Object-Based Image Analysis for semi-automated geological lineament detection in southwest England.* Computers and Geosciences, vol. 123, 2019, pp. 137–148. https://doi.org/10.1016/j.cageo.2018.11.005.

[33] Al-Nahmi F., Saddiqi O., Hilali A., Rhinane H., Baidder L., El Arabi H., Khanbari K.: *Application of remote sensing in geological mapping, case study Al Maghrabah area – Hajjah region, Yemen.* ISPRS Annals of the Photogrammetry, Remote Sensing and Spatial Information Sciences, vol. IV–4/W4, 2017, pp. 63–71. https://doi.org/10.5194/isprs-annals-IV-4-W4-63-2017.

[34] Bamoumen H., Aarab E., Soulaimani A.: *Evolution tectono-sédimentaire et magmatique des bassins viséen supérieur d'Azrou Khénifra et des Jebilet orientales (Meseta marocaine).* Estudios Geológicos, vol. 64(2), 2008, pp. 107–122. https://doi.org/10.3989/egeol.08642.020.

[35] Hoepffner C.: *La tectonique hercynienne dans l'Est du Maroc.* Université de Louis Pasteur, Strasbourg 1987 [thesis].

[36] Hoepffner C., Soulaimani A., Piqué A.: *The Moroccan Hercynides.* Journal of African Earth Sciences, vol. 43(1–3), 2005, pp. 144–165. https://doi.org/10.1016/j.jafrearsci.2005.09.002.

[37] Michard A.: *Eléments de Géologie Marocaine.* Notes et Mémoires du Service Géologique Maroc, vol. 252, Editions du Service Géologique du Maroc, Rabat 1976.

[38] Mrini Z., Rafi A., Duthou J.L., Vidal P.: *Chronologie Rb-Sr des granitoïdes hercyniens du Maroc: conséquences.* Bulletin de la Société Géologique de France, vol. 163(3), 1992, pp. 281–291.

[39] Diot H.: *Mise en place des granitoïdes hercyniens de la Meseta marocaine, étude structurale des massifs de Sebt de Brikine (Rehamna), de Zaër et d'Oulmès (Massif Central) et d'Aouli-Boumia (Haute Moulouya). Implications géodynamiques.* Université de Paul Sabatier, Toulouse 1989 [thesis].

[40] Michard A., Hoepffner C., Soulaimani A., Baidder L.: *The Variscan Belt.* [in:] Michard A., Saddiqi O., Chalouan A., Frizon de Lamotte D. (eds.), *Continental Evolution: The Geology of Morocco*, Lecture Notes in Earth Sciences, vol. 116, Springer, Berlin, Heidelberg, 2008, pp. 65–132. https://doi.org/10.1007/978-3-540-77076-3_3.

[41] Michard A., Soulaimani A., Hoepffner C., Ouanaimi H., Baidder L., Rjimati E.C., Saddiqi O.: *The South-Western Branch of the Variscan Belt: Evidence from Morocco.* Tectonophysics, vol. 492(1–4), 2010, pp. 1–24. https://doi.org/10.1016/j.tecto.2010.05.021.

[42] Giuliani G., Cheilletz A., Zimmermann J.L.: *The emplacement, geochemistry and petrogenesis of two central Morocco Hercynian granites. Geotectonic implications.* Journal of African Earth Sciences, vol. 9(3–4), 1989, pp. 617–629. https://doi.org/10.1016/0899-5362(89)90046-8.

[43] Haïmeur J., Chabane A., El Amrani El Hassani I.E.: *Analyse pétro-minéralogique des interactions granite-enclaves dans le pluton hercynien de Zaër (Maroc central); implications pétrogénétiques.* Bulletin de l'Institut Scientifique, Rabat, section Sciences de la Terre, vol. 25, 2003, pp. 1–29.

[44] Bouabdelli M.: *Tectonique et sédimentation dans un bassin orogénique: le sillon Viséen d'Azrou-Khenifra (Est du massif Hercynien Central du Maroc).* Université de Louis Pasteur, Strasbourg 1989 [thesis].

[45] Giuliani G.: *Découverte de minéralisations en Sn-W-Mo dans le pluton granitique hercynien des Zaërs (Massif Central marocain).* Comptes Rendus de l'Académie des Sciences Paris, vol. 290(D), 1980, pp. 1397–1399.

[46] Haïmeur J.: *Pétrologie et pétrologie structurale du pluton composite de Zaër: Implication à la pétrogenèse du système granitique hercynien du Maroc Central.* Université Ibn Tofaïl, Kénitra 2005 [thesis].

[47] Mahmood A.: *Etude pétrologique du granite hercynien des Zaër (Massif Central Marocain).* Université de Clermont-Ferrand, Clermont-Ferrand 1980 [thesis].

[48] Mrini Z.: *Age et origine des granitoïdes hercyniens du Maroc. Apport de la géochronologie et de la géochimie isotopique (Sr, Nd, Pb).* Université Blaise-Pascal, Clermont-Ferrand 1985 [thesis].

[49] Roy D.P., Wulder M.A., Loveland T.R., Woodcock C.E., Allen R.G., Anderson M.C., Helder D. et al.: *Landsat-8: Science and product vision for terrestrial global change research.* Remote Sensing of Environment, vol. 145, 2014, pp. 154–172. https://doi.org/10.1016/j.rse.2014.02.001.

[50] Wulder M.A., Loveland T.R., Roy D.P., Crawford C.J., Masek J.G., Woodcock C.E., Allen R.G. et al.: *Current status of Landsat program, science, and applications.* Remote Sensing of Environment, vol. 225, 2019, pp. 127–147. https://doi.org/10.1016/j.rse.2019.02.015.

[51] Loveland T.R., Irons J.R.: *Landsat 8: The plans, the reality, and the legacy.* Remote Sensing of Environment, vol. 185, 2016, pp. 1–6. https://doi.org/10.1016/j.rse.2016.07.033.

[52] Pandey P., Sharma L.N.: *Comparison of directional and non-directional filter techniques for lineament extraction using landsat-8 OLI to study active tectonics in parts of Northwestern HFT.* Research Journal of Recent Sciences, vol. 8(2), 2019, pp. 31–37.

[53] Abrams M., Tsu H., Hulley G., Iwao K., Pieri D., Cudahy T., Kargel J.: *The Advanced Spaceborne Thermal Emission and Reflection Radiometer (ASTER) after fifteen years: Review of global products.* International Journal of Applied Earth Observation and Geoinformation, vol. 38, 2015, pp. 292–301. https://doi.org/10.1016/j.jag.2015.01.013.

[54] Bedini E.: *Application of Advanced Spaceborne Thermal Emission and Reflection Radiometer (ASTER) multispectral imagery to mineral and lithologic mapping in southern West Greenland.* Journal of Hyperspectral Remote Sensing, vol. 8(2), 2018, pp. 47–59. https://doi.org/10.29150/jhrs.v8.2.p47-59.

[55] Obata K., Tsuchida S., Iwao K.: *Inter-band radiometric comparison and calibration of ASTER visible and near-infrared bands.* Remote Sensing, vol. 7(11), 2015, pp. 15140–15160. https://doi.org/10.3390/rs71115140.

[56] Kouyama T., Kato S., Kikuchi M., Sakuma F., Miura A., Tachikawa T., Tsuchida S. et al.: *Lunar calibration for ASTER VNIR and TIR with observations of the Moon in 2003 and 2017.* Remote Sensing, vol. 11(22), 2019, 2712. https://doi.org/10.3390/rs11222712.

[57] Obata K., Tsuchida S., Yamamoto H., Thome K.: *Cross-calibration between ASTER and MODIS visible to near-infrared bands for improvement of ASTER radiometric calibration.* Sensors, vol. 17(8), 2017, 1793. https://doi.org/10.3390/s17081793.

[58] Zhang X., Pazner M., Duke N.: *Lithologic and mineral information extraction for gold exploration using ASTER data in the south Chocolate Mountains (California).* ISPRS Journal of Photogrammetry and Remote Sensing, vol. 62(4), 2007, pp. 271–282. https://doi.org/10.1016/j.isprsjprs.2007.04.004.

[59] Bedini E.: *Mineral mapping in the Kap Simpson complex, central East Greenland, using HyMap and ASTER remote sensing data.* Advances in Space Research, vol. 47(1), 2011, pp. 60–73. https://doi.org/10.1016/j.asr.2010.08.021.

[60] El Janati M.: *Application of remotely sensed ASTER data in detecting alteration hosting Cu, Ag and Au bearing mineralized zones in Taghdout area, Central Anti-Atlas of Morocco.* Journal of African Earth Sciences, vol. 151, 2019, pp. 95–106. https://doi.org/10.1016/j.jafrearsci.2018.12.002.

[61] Fujisada H., Ono A.: *Observational performance of ASTER instrument on EOS-AM1 spacecraft.* Advances in Space Research, vol. 14(3), 1994, pp. 147–150. https://doi.org/10.1016/0273-1177(94)90207-0.

[62] Ge W., Cheng Q., Jing L., Armenakis C., Ding H.: *Lithological discrimination using ASTER and Sentinel-2A in the Shibanjing ophiolite complex of Beishan orogenic in Inner Mongolia, China.* Advances in Space Research, vol. 62(7), 2018, pp. 1702–1716. https://doi.org/10.1016/j.asr.2018.06.036.

[63] van der Meer F.D., van der Werff H.M.A., van Ruitenbeek F.J.A., Hecker C.A., Bakker W.H., Noomen M.F., van der Meijde M. et al.: *Multi- and hyperspectral geologic remote sensing: A review.* International Journal of Applied Earth Observation and Geoinformation, vol. 14(1), 2012, pp. 112–128. https://doi.org/10.1016/j.jag.2011.08.002.

[64] Gad S., Kusky T.: *ASTER spectral ratioing for lithological mapping in the Arabian-Nubian shield, the Neoproterozoic Wadi Kid area, Sinai, Egypt.* Gondwana Research, vol. 11(3), 2007, pp. 326–335. https://doi.org/10.1016/j.gr.2006.02.010.

[65] Hewson R.D., Cudahy T.J., Huntington J.F.: *Geologic and alteration mapping at Mt Fitton, South Australia, using ASTER satellite-borne data.* [in:] *IGARSS 2001: Proceedings: IEEE 2001 International Geoscience and Remote Sensing Symposium: Scanning the Present and Resolving the Future: 9–13 July, 2001, University of New South Wales, Sydney, Australia. Volume 2*, IEEE, Piscataway 2001, pp. 724–726. https://doi.org/10.1109/IGARSS.2001.976615.

[66] Rowan L.C., Mars J.C.: *Lithologic mapping in the Mountain Pass, California area using Advanced Spaceborne Thermal Emission and Reflection Radiometer (ASTER) data.* Remote Sensing of Environment, vol. 84(3), 2003, pp. 350–366. https://doi.org/10.1016/S0034-4257(02)00127-X.

[67] Rowan L.C., Schmidt R.G., Mars J.C.: *Distribution of hydrothermally altered rocks in the Reko Diq, Pakistan mineralized area based on spectral analysis of ASTER data.* Remote Sensing of Environment, vol. 104(1), 2006, pp. 74–87. https://doi.org/10.1016/j.rse.2006.05.014.

[68] Castillo J.A.A., Apan A.A., Maraseni T.N., Salmo III S.G.: *Estimation and mapping of above-ground biomass of mangrove forests and their replacement land uses in the Philippines using Sentinel imagery.* ISPRS Journal of Photogrammetry and Remote Sensing, vol. 134, 2017, pp. 70–85. https://doi.org/10.1016/j.isprsjprs.2017.10.016.

[69] Berger M., Moreno J., Johannessen J.A., Levelt P.F., Hanssen R.F.: *ESA's sentinel missions in support of Earth system science.* Remote Sensing of Environment, vol. 120, 2012, pp. 84–90. https://doi.org/10.1016/j.rse.2011.07.023.

[70] Drusch M., Del Bello U., Carlier S., Colin O., Fernandez V., Gascon F., Hoersch B. et al.: *Sentinel-2: ESA's Optical High-Resolution Mission for GMES Operational Services.* Remote Sensing of Environment, vol. 120, 2012, pp. 25–36. https://doi.org/10.1016/j.rse.2011.11.026.

[71] Unninayar S., Olsen L.M.: *Monitoring, observations, and remote sensing – global dimensions.* Reference Module in Earth Systems and Environmental Sciences, 2015, p. 31. https://doi.org/10.1016/B978-0-12-409548-9.09572-5.

[72] Li J., Roy D.P.: *A Global Analysis of Sentinel-2A, Sentinel-2B and Landsat-8 data revisit intervals and implications for terrestrial monitoring.* Remote Sensing, vol. 9(9), 2017, 902. https://doi.org/10.3390/rs9090902.

[73] Ge W., Cheng Q., Tang Y., Jing L., Gao C.: *Lithological classification using Sentinel-2A data in the Shibanjing Ophiolite Complex in Inner Mongolia, China.* Remote Sensing, vol. 10(4), 2018, 638. https://doi.org/10.3390/rs10040638.

[74] van der Werff H., van der Meer F.: *Sentinel-2A MSI and Landsat 8 OLI provide data continuity for geological remote sensing.* Remote Sensing, vol. 8(11), 2016, 883. https://doi.org/10.3390/rs8110883.

[75] Bourbigot M., Johnsen H., Piantanida R.: *Sentinel-1 product definition. ESA.* Document Number: S1-RS-MDA-52-7440, 25 March 2016.

[76] Kaplan G., Avdan U.: *Sentinel-1 and Sentinel-2 data fusion for wetlands mapping: Balikdami, Turkey.* ISPRS – International Archives of the Photogrammetry, Remote Sensing and Spatial Information Sciences, vol. XLII-3, 2018, pp. 729–734. https://doi.org/10.5194/isprs-archives-XLII-3-729-2018.

[77] Tavares P.A., Beltrão N.E.S., Guimarães U.S., Teodoro A.C.: *Integration of Sentinel-1 and Sentinel-2 for classification and LULC mapping in the urban area of Belém, Eastern Brazilian Amazon.* Sensors, vol. 19(5), 2019, 1140. https://doi.org/10.3390/s19051140.

[78] Shebl A., Csámer Á.: *Reappraisal of DEMs, Radar and optical datasets in lineaments extraction with emphasis on the spatial context.* Remote Sensing Applications: Society and Environment, vol. 24, 2021, 100617. https://doi.org/10.1016/j.rsase.2021.100617.

[79] Abrams M., Crippen R., Fujisada H.: *ASTER Global Digital Elevation Model (GDEM) and ASTER Global Water Body Dataset (ASTWBD).* Remote Sensing, vol. 12(7), 2020, 1156. https://doi.org/10.3390/rs12071156.

[80] Adiri Z., El Harti A., Jellouli A., Lhissou R., Maacha L., Azmi M., Zouhair M., Bachaoui E.M.: *Comparison of Landsat-8, ASTER and Sentinel 1 satellite remote sensing data in automatic lineaments extraction: A case study of Sidi Flah-Bouskour inlier, Moroccan Anti Atlas.* Advances in Space Research, vol. 60(11), 2017, pp. 2355–2367. https://doi.org/10.1016/j.asr.2017.09.006.

[81] Jellouli A., El Harti A., Adiri Z., Chakouri M., El Hachimi J., Bachaoui E.M.: *Application of optical and radar satellite images for mapping tectonic lineaments in kerdous inlier of the Anti-Atlas belt, Morocco.* Remote Sensing Applications: Society and Environment, vol. 22, 2021, 100509. https://doi.org/10.1016/j.rsase.2021.100509.

[82] Mahmood A.: *Emplacement of the zoned Zaer pluton, Morocco.* Geological Society of America Bulletin, vol. 96(7), 1985, pp. 931–939. https://doi.org/10.1130/0016-7606(1985)96<931:EOTZZP>2.0.CO;2.

[83] Pour A.B., Park T.Y.S., Park Y., Hong J.K., Muslim A.M., Läufer A., Crispini L. et al.: *Landsat-8, Advanced Spaceborne Thermal Emission and Reflection Radiometer, and WorldView-3 multispectral satellite imagery for prospecting copper-gold mineralization in the Northeastern Inglefield Mobile Belt (IMB), Northwest Greenland.* Remote Sensing, vol. 11(20), 2019, 2430. https://doi.org/10.3390/rs11202430.

[84] Pour A.B., Hashim M.: *Application of Landsat-8 and ALOS-2 data for structural and landslide hazard mapping in Kelantan, Malaysia.* Natural Hazards and Earth System Sciences, vol. 17, 2017, pp. 1285–1303. https://doi.org/10.5194/nhess-17-1285-2017.

[85] Meyer D., Siemonsma D., Brooks B., Johnson L.: *Advanced Spaceborne Thermal Emission and Reflection Radiometer level 1 precision terrain corrected registered at-sensor radiance (AST_L1T) product, algorithm theoretical basis document*. Open-File Report 2015-1171, Reston, VA, 2015. https://doi.org/10.3133/ofr20151171.

[86] Cooley T., Anderson G.P., Felde G.W., Hoke M.L., Ratkowski A.J., Chetwynd J.H., Gardner J.A. et al.: *FLAASH, a MODTRAN4-based atmospheric correction algorithm, its application and validation.* [in:] *IGARSS 2002: IEEE International Geoscience and Remote Sensing Symposium, Toronto, Ontario, Canada, 24–28 June 2002. Volume 3*, IEEE, Piscataway 2002, pp. 1414–1418. https://doi.org/10.1109/IGARSS.2002.1026134.

[87] Phiri D., Morgenroth J., Xu C., Hermosilla T.: *Effects of pre-processing methods on Landsat OLI-8 land cover classification using OBIA and random forests classifier.* International Journal of Applied Earth Observation and Geoinformation, vol. 73, 2018, pp. 170–178. https://doi.org/10.1016/j.jag.2018.06.014.

[88] Laben C.A., Brower B.V.: *Process for enhancing the spatial resolution of multispectral imagery using pan-sharpening*. Patent no. 6011875, date of publication January 4, 2000.

[89] Maurer T.: *How to pan-sharpen images using the Gram-Schmidt pan-sharpen method – a recipe.* International Archives of the Photogrammetry, Remote Sensing and Spatial Information Sciences, vol. XL-1/W1, 2013, pp. 239–244. https://doi.org/10.5194/isprsarchives-XL-1-W1-239-2013.

[90] Amer R., Kusky T., El Mezayen A.: *Remote sensing detection of gold related alteration zones in Um Rus area, Central Eastern Desert of Egypt.* Advances in Space Research, vol. 49(1), 2012, pp. 121–134. https://doi.org/10.1016/j.asr.2011.09.024.

[91] Yang M., Kang L., Chen H., Zhou M., Zhang J.: *Lithological mapping of East Tianshan area using integrated data fused by Chinese GF-1 PAN and ASTER multi-spectral data*. Open Geosciences, vol. 10(1), 2018, pp. 532–543. https://doi.org/10.1515/geo-2018-0042.

[92] Vasilakos C., Kavroudakis D., Georganta A.: *Machine learning classification ensemble of multitemporal Sentinel-2 images: The case of a mixed Mediterranean ecosystem.* Remote Sensing, vol. 12(12), 2020, 2005. https://doi.org/10.3390/rs12122005.

[93] Louis J., Pflug B., Main-Knorn M., Debaecker V., Mueller-Wilm U., Iannone R.Q., Giuseppe Cadau E. et al.: *Sentinel-2 global surface reflectance level-2A product generated with Sen2Cor.* [in:] *IGARSS 2019 – 2019 IEEE International Geoscience and Remote Sensing Symposium, Yokohama, Japan, 28 July – 2 August 2019*, IEEE, Piscataway 2000, pp. 8522–8525. https://doi.org/10.1109/IGARSS.2019.8898540.

[94] Vuolo F., Żółtak M., Pipitone C., Zappa L., Wenng H., Immitzer M., Weiss M. et al.: *Data service platform for Sentinel-2 surface reflectance and value-added products: System use and examples.* Remote Sensing, vol. 8(11), 2016, 938. https://doi.org/10.3390/rs8110938.

[95] Filipponi F.: *Sentinel-1 GRD preprocessing workflow.* Proceedings, vol. 18(1), 2019, 11. https://doi.org/10.3390/ECRS-3-06201.

[96] Twele A., Cao W., Plank S., Martinis S.: *Sentinel-1-based flood mapping: a fully automated processing chain.* International Journal of Remote Sensing, vol. 37(13), 2016, pp. 2990–3004. https://doi.org/10.1080/01431161.2016.1192304.

[97] Crósta A.P., De Souza Filho C.R., Azevedo F., Brodie C.: *Targeting key alteration minerals in epithermal deposits in Patagonia, Argentina, using ASTER imagery and principal component analysis.* International Journal of Remote Sensing, vol. 24(21), 2003, pp. 4233–4240. https://doi.org/10.1080/0143116031000152291.

[98] Li N.: *Textural and rule-based lithological classification of remote sensing data, and geological mapping in Southwestern Prieska sub-basin, Transvaal Supergroup, South Africa.* Ludwig-Maximilians-Universität München, Munich 2010 [thesis].

[99] Pour A.B., Hashim M.: *The application of ASTER remote sensing data to porphyry copper and epithermal gold deposits*. Ore Geology Reviews, vol. 44, 2012, pp. 1–9. https://doi.org/10.1016/j.oregeorev.2011.09.009.

[100] Singh A., Harrison A.: *Standardized principal components.* International Journal of Remote Sensing, vol. 6, 1985, pp. 883–896. https://doi.org/10.1080/01431168508948511.

[101] Gabr S., Ghulam A., Kusky T.: *Detecting areas of high-potential gold mineralization using ASTER data.* Ore Geology Reviews, vol. 38(1–2), 2010, pp. 59–69. https://doi.org/10.1016/j.oregeorev.2010.05.007.

[102] Amer R., Kusky T., Ghulam A.: *Lithological mapping in the Central Eastern Desert of Egypt using ASTER data.* Journal of African Earth Sciences, vol. 56(2–3), 2010, pp. 75–82. https://doi.org/10.1016/j.jafrearsci.2009.06.004.

[103] Walsh S.J., Mynar F.: *Landsat digital enhancements for lineament detection.* Environmental Geology and Water Sciences, vol. 8(3), 1986, pp. 123–128. https://doi.org/10.1007/BF02509898.

[104] Paganelli F., Grunsky E.C., Richards J.P., Pryde R.: *Use of RADARSAT-1 principal component imagery for structural mapping: a case study in the Buffalo Head Hills area, northern central Alberta, Canada.* Canadian Journal of Remote Sensing, vol. 29(1), 2003, pp. 111–140. https://doi.org/10.5589/m02-084.

[105] Si Mhamdi H., Raji M., Oukassou M.: *Utilisation de la télédétection dans la cartographie automatique des linéaments géologiques du granitoïde de Tichka (Haut Atlas Occidental).* European Journal of Scientific Research, vol. 142(4), 2016, pp. 321–333.

[106] Pour A.B., Hashim M.: *Structural mapping using PALSAR data in the Central Gold Belt, Peninsular Malaysia.* Ore Geology Reviews, vol. 64, 2015, pp. 13–22. https://doi.org/10.1016/j.oregeorev.2014.06.011.

[107] Marston B.E., Jenny B.: *Improving the representation of major landforms in analytical relief shading.* International Journal of Geographical Information Science, vol. 29(7), 2015, pp. 1144–1165. https://doi.org/10.1080/13658816.2015.1009911.

[108] Alhirmizy S.: *Automatic mapping of lineaments using shaded relief images derived from Digital Elevation Model (DEM) in Kirkuk Northeast Iraq.* International Journal of Science and Research, vol. 4(5), 2015, pp. 2228–2233.

[109] Li X., Zhang Y., Jin X., He Q., Zhang X.: *Comparison of digital elevation models and relevant derived attributes.* Journal of Applied Remote Sensing, vol. 11(4), 2017, 046027. https://doi.org/10.1117/1.JRS.11.046027.

[110] Mahalingam R., Olsen M.J.: *Evaluation of the influence of source and spatial resolution of DEMs on derivative products used in landslide mapping.* Geomatics, Natural Hazards and Risk, vol. 7(6), 2015, pp. 1835–1855. https://doi.org/10.1080/19475705.2015.1115431.

[111] Ganas A., Pavlides S., Karastathis V.: *DEM-based morphometry of range-front escarpments in Attica, central Greece, and its relation to fault slip rates.* Geomorphology, vol. 65(3–4), 2005, pp. 301–319. https://doi.org/10.1016/j.geomorph.2004.09.006.

[112] Nkono C., Féménias O., Lesne A., Mercier J.C., Demaiffe D.: *Fractal analysis of lineaments in equatorial Africa: Insights on lithospheric structure.* Open Journal of Geology, vol. 3(3), 2013, pp. 157–168. https://doi.org/10.4236/ojg.2013.33019.

[113] Pandey P., Sharma L.N.: *Image processing techniques applied to satellite data for extracting lineaments using PCI Geomatica and their morphotectonic interpretation in the parts of Northwestern Himalayan Frontal Thrust.* Journal of the Indian Society of Remote Sensing, vol. 47(5), 2019, pp. 809–820. https://doi.org/10.1007/s12524-019-00962-2.

[114] Papadaki E.S., Mertikas S.P., Sarris A.: *Identification of lineaments with possible structural origin using ASTER images and DEM derived products in Western Crete, Greece.* EARSeL eProceedings, vol. 10(1), 2011, pp. 9–26.

[115] Phiri D., Simwanda M., Salekin S., Nyirenda V.R., Murayama Y., Ranagalage M.: *Sentinel-2 data for land cover/use mapping: A review.* Remote Sensing, vol. 12(14), 2020, 2291. https://doi.org/10.3390/rs12142291.

[116] Mallast U., Gloaguen R., Geyer S., Rödiger T., Siebert C.: *Derivation of groundwater flow-paths based on semi-automatic extraction of lineaments from remote sensing data.* Hydrology and Earth System Sciences, vol. 15(8), 2011, pp. 2665–2678. https://doi.org/10.5194/hess-15-2665-2011.

[117] Bruning J.N., Gierke J.S., Maclean A.L.: *An approach to lineament analysis for groundwater exploration in Nicaragua.* Photogrammetric Engineering and Remote Sensing, vol. 77(5), 2011, pp. 509–519. https://doi.org/10.14358/PERS.77.5.509.

[118] Radaideh O.M.A., Grasemann B., Melichar R., Mosar J.: *Detection and analysis of morphotectonic features utilizing satellite remote sensing and GIS: An example in SW Jordan.* Geomorphology, vol. 275, 2016, pp. 58–79. https://doi.org/10.1016/j.geomorph.2016.09.033.

[119] Casas A.M., Cortés A.L., Maestro A., Soriano M.A., Riaguas A., Bernal J.: LINDENS: *A program for lineament length and density analysis.* Computers and Geosciences, vol. 26(9–10), 2000, pp. 1011–1022. https://doi.org/10.1016/S0098-3004(00)00017-0.

[120] Ferré E.C., Yeh E.-C., Chou Y.-M., Kuo R.L., Chu H.-T., Korren C.S.: *Brushlines in fault pseudotachylytes: A new criterion for coseismic slip direction.* Geology, vol. 44(5), 2016, pp. 395–398. https://doi.org/10.1130/G37751.1.

[121] Kearse J., Kaneko Y.: *On-fault geological fingerprint of earthquake rupture direction.* Journal of Geophysical Research: Solid Earth, vol. 125(9), 2020, e2020JB019863. https://doi.org/10.1029/2020JB019863.

[122] Nováková L., Novák P., Brož M., Sosna K., Pitrák M., Kasíková J., Rukavičková L., Maňák L.: *The results of borehole acoustic imaging from a granite in the Jihlava District, Czech Republic: Implications for structural geological research.* Journal of Geography and Geology, vol. 4(4), 2012, pp. 92–101. https://doi.org/10.5539/jgg.v4n4p92.

[123] Kearse J., Kaneko Y., Little T., Van Dissen, R.: *Curved slickenlines preserve direction of rupture propagation.* Geology, vol. 47(9), 2019, pp. 838–842. https://doi.org/10.1130/G46563.1.

[124] Lagarde J.L., Ait Ayad N., Ait Omar S., Chemsseddoha A., Saquaque A.: *Plutons granitiques tardi carbonifères marqueurs de la déformation crustale. L'exemple de la Meseta marocaine.* Comptes Rendus de l'Académie des Sciences Paris, vol. 309(II), 1989, pp. 291–296.

[125] Lagarde J.L., Ait Omar S., Roddaz B.: *Structural characteristics of granitic plutons emplaced during weak regional deformation: examples from late Carboniferous plutons, Morocco.* Journal of Structural Geology, vol. 12(7), 1990, pp. 805–821. https://doi.org/10.1016/0191-8141(90)90056-5.

[126] Matte P.: *La chaine varisque parmi les chaines paléozoïques péri atlantiques, modèle d'évolution et position des grands blocs continentaux au Permo-Carbonifère.* Bulletin de la Société Géologique de France, vol. II(1), 1986, pp. 9–24. https://doi.org/10.2113/gssgfbull.II.1.9.

[127] Lagarde J.L.: *Cisaillements ductiles et plutons granitiques contemporains de la déformation hercynienne de la meseta marocaine.* Hercynica, vol. 1, 1985, pp. 29–37.

[128] Piqué A., Michard A.: *Moroccan Hercynides; a synopsis; the Paleozoic sedimentary and tectonic evolution at the northern margin of West Africa.* American Journal of Science, vol. 289(3), 1989, pp. 286–330. https://doi.org/10.2475/ajs.289.3.286.

[129] Saidi A.: *Paléochamps de contraintes et importance de l'héritage hercynien dans la structuration du Maroc central septentrional du Permien à l'actue*l. Université de Mohamed V, Rabat 1996 [thesis].